Geometric properties of streamlines in turbulent wall-flows

Rina Perven

Department of Mechanical Engineering
University of Melbourne

A thesis submitted in total fulfilment of the requirements of the degree of Master of Philosophy

December 2019

Declaration of Authorship

This is to certify that:

- this thesis comprises only my original work except where indicated,
- due acknowledgement has been made in the text to all other material used,
- this thesis is fewer than 50 000 words in length, exclusive of tables, bibliographies and appendices.

Rina Perven 15 August 2019

Abstract

Streamline geometry has been studied in case of turbulent wall flows. Complex but coherent motions form and rapidly evolve within wall-bounded turbulent flows. Research over the past two decades broadly indicates that the momentum transported across the flow derives from the dynamics underlying these coherent motions. This spatial organization, and its inherent connection to the dynamics, motivates the present research.

The local streamline geometry pertaining to curvature (κ) and torsion (τ) has apparent connection to the dynamics of the flow. The present results indicate that these geometrical properties change significantly with wall-normal position. One part of this research is thus to clarify the observed changes in the streamline geometry with the known structure and scaling behaviours of the mean momentum equation. Towards this aim, the curvature and torsion of the streamlines at each point in the volume of existing boundary layers and channel DNS has been computed. The computation of κ and τ arise from the local construction of the Frenet-Serret coordinate frame. The present methods for estimating κ includes components of curvature in the streamwise, wall-normal and spanwise direction.

The analysis shows that even though the mean wall-normal velocity is zero (e.g., for channel flow), the wall-normal curvature component shows a notable positive peak close to the wall. This arises from the strong wallward flow followed by a weak movement of the streamlines away from the wall. The correlation coefficient and the conditional average of the wall-normal velocity corresponding to the wall-normal curvature exhibit an anti-correlation between them.

The probability density function of the curvatures have been calculated at some wall-normal locations of interest and compared with a scaling of the exponent of -4 for both total and fluctuating field. This scaling of curvature values describes the geometric features of the length scales that are smaller than the Kolmogorov scale. The onset of this scaling with wall distance has a potential connection to the three-dimensionalization of the vorticity field and the stagnation points structure

in the inertial domain. In this region, the mean radius of curvature scales like Taylor microscale. The probability density functions of the wall-normal curvature show that high curvature regions similar to those in isotropic flow begin to appear outside the viscous wall layer.

The standard deviation for torsion exhibits a decreasing effect with distance from the wall. The torsion to curvature ratio reveals the intensity of out of plane motion of the streamlines relative to their in-plane bending. The joint pdf of curvature with velocity magnitude supports the notion that large curvature values correspond to the region near a stagnation point. Furthermore, the joint pdf results between curvature components reveal the orientation of the streamlines at different wall-normal locations. Overall the curvature and torsion statistics examined thus far point to intriguing correlations with the four layer structure associated with known structure of the vorticity field in turbulent wall-flows.

Contents

List of Figures

Acknowledgements

First of all, I convey my heartiest gratefulness to the Almighty to set-up my luck in academic areas with some great achievements.

I would like to extend my sincerest gratitude to my supervisors, Prof. Joseph Klewicki and Dr. Jimmy Philip, whose kind constant support and guidance are invaluable. Their expertise suggestions towards wall-flow turbulence have helped to build my perspective in this field. I am very fortunate to have had the opportunity to work with them.

I would also like to thank my committee chair Prof. Richard Sandberg and my committee member A/Prof. Daniel Chung for their valuable remarks and suggestions during my progress review meetings.

I would like to heartily gratitude to Cindy Klewicki. I still remember the first day we met while helping me to find accommodation. Her mother-like caring that time was beyond my expectation. Cordial thanks for sharing the nice moments with coffee every time we met.

I would also like to thank my friends and colleagues in the fluid mechanics group. Special thanks to Dr. Spencer Zimmermann, Dr. Caleb Morrill-Winter, Dr. Dileep Chandran, Vijaya Gudla, Dr. Charitha deSilva, Dr. Rio Baidya, Dr. Dougie Squire, Dr. Kevin and Dr. Milad Samie for the countless informative discussions and their willingness to share their expertise.

I would like to acknowledge Ms. Emma Mitchell and Jan may for all the official support. I will never forget the affection and caring of Ms. Emma Mitchell not only scheduling my meeting but also other caring help. I would like to thank to all other friends and staff of Mechanical Engineering department.

I also like to heartiest thank to the MSE Graduate Research Team specially, Petra Van Nieuwenhoven, Sarah Gloger, Kate Hale and Jutta Besold for their immense help during my candidature time. I would like to thank all of my Bangladeshi friends living here who gave a family life touch and cared me a lot.

Finally, I would like to thank my family for their support, encouragement, and understanding me; specially my mother Anjuara Begum, my husband Abu Saleh Ahmad, and my brother Md. Razu Zomaddar. This degree is a very special one to me as I got my soulmate and we married each other in between. During the crucial stages of my degree, he was just amazing to support and motivate me in every aspect he could. I love you always and will be loving you through the rest of my life and hereafter as well. There is no words to convey my gratefulness to my mother who are just living for us after being widow at the age of 30. —this work is dedicated to you “Ma”.

Nomenclature

Notation

y^+	Wall-normal position
t	Unit tangent vector
r	Radius
W	Width of each layer
k	Von Kármán constant
η	Kolmogorov length scale
$\kappa_x, \kappa_y, \kappa_z$	streamwise, wall-normal and spanwise curvature components
uv	Reynolds shear stress
V	Velocity magnitude
$\mathbf{T}$	Tangent vector
s	Arclength of a curve
$\mathbf{N}$	Normal vector
Re	Reynolds number
Re_τ	Reynolds number based on friction velocity
R_{v,κ_y}	Correletaion coefficient of wall-nomal velocity and curvature components
r_{v,κ_y}	Correletaion function of wall-nomal velocity and curvature components
U	Mean streamwise velocity
u_∞	Freestream velocity
u_τ	Mean friction velocity
u, v, w	Streamwise, wall-normal and spanwise velocity fluctuations

h	Step size between two point on the streamline
$\mathbf{B}$	Binormal vector
x, y, z	Streamwise, wall-normal and spanwise directions

Greek

κ	Curvature
τ	Torsion
δ	Boundary layer thickness or Channel half hight
δ_{99}	Boundary layer thickness based on 99% of U_∞
$\mathfrak{K}$	Turbulence kinetic energy
ϵ	turbulent energy dissipation
η	Kolmogorov length scale
λ	Taylor microscale
ν	Kinematic viscosity
ρ	Density of fluid
τ_w	Mean shear stress at the wall
u_τ	Friction velocity
ν	Kinematic viscosity
ρ	Mass density
λ_ϵ	Taylor microscale using isotropic consideration
β	Streamline
χ^2	Chi square distribution
σ_τ	Standard deviation of torsion
σ_v	Standard deviation of wall-normal velocity
κ_g	Gaussian curvature
σ_κ	Standard deviation of curvature

Abbreviation

PG	Pressure gradient
VF	Viscous force

pdf	Probability density function
AEH	Attached eddy hypothesis
COMP	Composite
DNS	Direct numerical simulation
TI	Turbulent inertia
RANS	Reynolds Average Navier-Stokes equation
NSE	Navier-Stokes Equation
LSM	Large-scale motion
LCS	Linear coherence spectrum
PIV	Particle image velocimetry
VLSM	Very-large-scale motion
MMB	Mean momentum balance

Chapter 1

Introduction

Turbulence is a property of fluid (liquid or gas) flows. It can be characterized by listing some of its attributes, such as irregularity, diffusivity, large Reynolds numbers, three-dimensional vorticity fluctuations, high dissipation, etc. (e.g. see Tennekes & Lumley [1972]). Laminar flows become turbulent if the Reynolds number is sufficiently high, e.g. $\sim$ 2000 (for pipe flow). The sources of energy for turbulent velocity fluctuations are the shear in the mean flow, buoyancy, etc. In the case of turbulent boundary-layer flows, the characteristic velocity of the turbulence is typically about 1/30 of the free-stream flow speed in laboratory scale flows. The classical model for turbulent flows is that the majority of the kinetic energy is associated with large-scale motions while the majority of the vorticity is associated with small-scale motions. This segregation of scales has implications regarding the geometric features of the underlying motions. Namely, turbulent flow with low Reynolds number has a relatively "rough" small scale structure. A basic quality of turbulent motion influenced by this structure is the enhancement of momentum transfer. When two turbulent flows have the same integral scale but the different Reynolds number then a fundamental difference is the relative size of the smallest eddies. All of these features present some of the general behaviours of the turbulent flow of a fluid.

When there is a fluid flow with a certain velocity over a stationary surface or a wall, then at the wall the velocity of the flow will turn to the wall velocity (zero) to satisfy the no-slip condition. The velocity increases with distance from the wall. and becomes the free-stream velocity after a particular distance. The distance from the wall to this particular location is defined as the boundary layer thickness. The flow within this region is known as a "wall-bounded flow" or "boundary layer flow". Wall-flow dynamics are of pervasive scientific and technological importance. In this research, the wall-bounded flows are considered for all the analyses.

This thesis represents, an effort to better understand the flow structure by analyzing the geometric properties of the flow field, and to draw potential connections between these geometric properties and the dynamics of the flow. Here, the geometric properties are related to the curvature (κ) and torsion (τ) of the streamlines, where a streamline is defined by the curve that is instantaneously tangent to the

velocity of the flow. Curvature measures the deviation from a straight line i.e. bending of the streamline and torsion is the out of plane motion i.e. twisting of the streamline.

1.1 Motivation

In the case of wall-bounded flows, the predominant features tangential to the wall result because the fluid particles stick to the wall. This no-slip condition affects a velocity variation with distance from the wall. Turbulent wall-flows contain a complex array of eddying motions that support the long-time statistical structure of the flow. Nonlinear interactions underlie the spatial and temporal fluctuations of these eddying motions; having effects that are notoriously difficult to predict or control. **The present research seeks to clarify properties of this spatial fluctuating motion by analysing the flow geometry.**

Turbulent wall-flows are technologically ubiquitous, as the transport of heat, mass and momentum dictated by these flows substantially impact numerous processes of engineering, societal, and commercial importance. Wall-flows at high Reynolds numbers are especially important, e.g. Klewicki [2010]. Technological applications include those in manufacturing and power generation, while the dynamics of turbulent wall-flows are also directly linked to the primary cost of materials transport and transportation. Namely, these dynamics are responsible for much of the fuel consumed by aircraft, ships, and industrial piping networks. The pervasive importance of turbulent wall-flow dynamics offers engineers opportunities to impart large positive impact through only small percentage improvements. In this regard, a wealth of existing evidence indicates that more advanced knowledge of the robust features of wall-turbulence would significantly further efforts pertaining to reliable wall-flow prediction and control (e.g. Klewicki [2010], Marusic *et al.* [2010], Smits *et al.* [2011]). An important quality of these features is that, while they are operative at all Reynolds numbers, they emerge with increasing clarity as the Reynolds number becomes large. **There is a broad need to elucidate the qualities characteristic of these asymptotic dynamical features, as their prediction and modification are key to engineering design and control applications.**

Exposing and characterizing the robust features of wall-turbulence presents a number of challenges. Unfortunately, the most significant of these also become increasingly acute as the Reynolds number becomes large (Klewicki [2010]). The crux of the matter is that the dynamics are governed by the Navier-Stokes equation (NSE) as constrained by the no-slip boundary condition at the wall. The dynamically relevant spatial and temporal interactions that arise from the nonlinearities of the NSE are famously complex and are further complicated by an increasing range with Reynolds number, and anisotropic vorticity stretching near the wall. Effective prediction or control of these flows requires mechanistically faithful representations of their inherent complexities, while practical constraints demand that these representations be contained in computationally efficient mathematical

models-especially as the Reynolds number gets large and the range of relevant scales increases. Wall-flow dynamics are, however, only accessible via observed flow field realizations. Thus, mathematically compact constructions that guide the analysis of these increasingly enormous data sets provide an attractive means by which flow field realization's can be comprehended and efficiently represented in dynamical models. This is especially the case if the underlying framework retains the connection to the NSE. **The proposed research seeks to elucidate the flow field realization by analyzing the flow geometries and clarify the nature and origin of recently observed connections between the geometry and dynamics of wall-turbulence**.

This research includes investigating velocity field streamlines curvature and torsion statistics in wall-turbulence. These streamlines properties are known to be dynamically significant (Wu *et al.* [2007]), and provide a mathematically well-defined measure of flow structure. In comparison to particle trajectories, however, relatively few studies have investigated streamline curvature and torsion directly, e.g., Wang [2010], Schaefer [2012] and beyond the present low Reynolds number results, none in wall-turbulence. Relative to log layer structure, it is noted that streamline curvature becomes very large in the vicinity of stagnation points (Schaefer [2012]). This may have a connection to studies indicating that the spatial distribution of stagnation points relates to the value of the leading coefficient in the log law formula for the mean velocity, i.e. von Kármán's coefficient (k), (Dallas *et al.* [2009]). Conversely, within the theoretical framework presented by Klewicki *et al.* [2014], k directly connects to the self-similar geometric structure of the flow. **Collectively, such observations motivate the investigation of flow field geometry using both statistical measures, and by characterizing the instantaneous streamline properties.**

1.2 Aims

In summary, this research aims to:

- clarify mechanisms underlying the apparent connections between geometry and dynamics, and the degree to which they are reflected in the instantaneous motions.
- analyse of the streamline geometries (curvature and torsion) in case of the wall-bounded turbulence and discuss both viscous and the wall-blocking effects.
- conceptualize the flow structure by analyzing the instantaneous streamline curvature and torsion properties.
- investigate the curvature and torsion statistics, and relate the mean curvature statistics to the mechanisms of vorticity stretching and reorientation as analyzed by Klewicki [2013*a*]

- test for the existence of a -4 scaling (proposed by Schaefer [2012]) for the large curvature values and compare the onset of this scaling with the Kolmogorov length scale
- compare the radius of curvature with the Taylor microscale in the inertial layer and relate this to the stagnation points intermediate distance studied by Goto & Vassilicos [2009].
- characterize stagnation points by analysing curvature values and relate to the findings by Schaefer [2012] and Dallas *et al.* [2009].

Thus the proposed effort aims to elucidate the origin of recent analyses and observations that point to compelling connections between the dynamics of the flow, and geometric properties of the turbulent motions responsible for this dynamics. Apparent connections include those involving the structure of the solutions to the time-averaged equations of motion, geometric properties inherent to the mean flow structure, as well as those reflected in surprisingly rudimentary statistics. The primary focus is on the flow behaviors within the self-similar inertial region unique to turbulent wall-flows. Here the mean velocity is well-approximated by a logarithmic equation (e.g. Marusic *et al.* [2013]), and the mean flow equations admit an asymptotic similarity solution (e.g. Klewicki [2013*b*]). While analytical and empirical evidence point to firm connections between geometry and dynamics on this inertial domain, the mechanistic origins of this evidence are unknown. This is where the proposed research broadly seeks to make a contribution.

In this regard, the broad outline of this thesis is as follows: Chapter 2 presents the relevant definitions and background work including the description of the exponent of -4 scaling and stagnation point structure; which will be extensively used in the discussion of the last three aims. Chapter 3 provides the methodology of computation including the preliminary plots for comparison of different calculation methods and code validation. Chapter 4 outlines the statistical results of curvature and torsion including the relations with previous findings. Finally, chapter 5 contains the general findings and summarization of the present research.

Publications and manuscripts

(*i*) Perven, R., Philip, J., & Klewicki, J. 2019 Statistical properties of streamline geometry in turbulent wall-flows. *Physical Review Fluids* (Close to submit.)

Conference presentations

(*i*) Perven, R., Philip, J., & Klewicki, J. 2017 Statistical properties of streamline curvature and torsion in turbulent wall-flows. Presented in poster presentation *Frontiers in Turbulence KRS70 at Denver Symposium*, vol. 60. Denver, CO, USA

(*ii*) Perven, R., Philip, J., & Klewicki, J. 2019 Statistics of streamline geometry in wall-bounded turbulence. Presented for oral presentation *17TH European Turbulence Conference* that held on 3-6 September 2019, Torino, Italy

Chapter 2

Relevant literature review

This chapter includes the technical definitions with relevant literature review. The important ingredients of this present study draw upon to compare and resemble with (*i*) the leading order mean force balance in turbulent wall-flows (*ii*) the previously documented behaviour of streamline curvature probability density functions in isotropic turbulent flows [Schaefer, 2012], and (*iii*) the characteristic length scales and the geometric and scaling implications associated with the distributions of stagnation points in the fluctuating velocity field [Dallas *et al.*, 2009]. The aim here is not to present the extensive review of related prior studies but to provide the sufficient base for the reader to follow the analysis and discussion for this thesis. The broader intent of this study is to find the potential connection between the geometry and dynamics of wall-bounded turbulent flows. In this regard, the current chapter first includes the relevant literature on the mean dynamical structure and then the relevant literature on streamline geometry. To summarize, the last part of this chapter covers the significant connection of the previous literature to the present study.

2.1 Wall-bounded turbulent flows

In general, wall-bounded turbulence is a type of flow that is attached to a wall. Some general examples of the wall-bounded flows are the boundary layer, channel, and pipe flows. Complex motions form and rapidly evolve within the sufficiently high speed flow of a fluid (liquid or gas) tangential to a solid surface. Such flows are called turbulent wall-flows, and the momentum transported across them derives from the dynamics underlying their complex motions. Accordingly, engineers and scientists have the need to better characterize, predict, and control these dynamics. This need is particularly acute as the primary dynamical parameter, Reynolds number, becomes large. High Reynolds number wall-flows have greatest relevance to long-standing challenges pertaining to energy and environmental sustainability. Unfortunately, these flows are also the most difficult to study ([Klewicki, 2010]). With increasing Reynolds number, wall-flows exhibit emergent qualities that reflect

their essential physics at all Reynolds numbers. There is a broad need to elucidate the qualities characteristic of the asymptotic dynamical state, as their prediction and modification are key to engineering design and control applications.

Unlike isotropic flow with zero mean velocity, the present wall-bounded flows are not Galilean invariant. Galilean invariance however, is not a relevant consideration in the present flow. This is because the no-slip boundary condition breaks this invariance [Huerre & Monkewitz, 1990].

2.2 Relevant literature

Coherent motions have long been known to populate turbulent wall-flows through a process of continual formation, evolution, and obliteration [Klewicki, 2010, Marusic *et al.*, 2010, Robinson, 1991]. This spatio-temporal recurrence of motions is related with identifiably recognizable spatial organization and similar evolutionary features. An intriguing motivation for deeper investigation is associated with the potential to use these motions, in some systematic manner, as a basis for simplified descriptions that capture the essential elements of wall-flow dynamics e.g. [Jeong *et al.*, 1997, Sharma & McKeon, 2013]. Indeed, in a statistical sense, this underlying spatial organization leads many to strongly suspect that the long-recognized self-similar scaling properties of turbulent wall flows connects the geometry and dynamics of these instantaneously realized motions [Klewicki *et al.*, 2014]. As with many studies of turbulence, a primary gap in our present understanding pertains to these connections between statistical behaviours of the geometric features and the underlying instantaneous dynamics. The present study addresses aspects of this knowledge gap by quantifying statistical properties associated with the differential geometry measures of curvature and (to a much lesser degree) torsion of the streamline patterns in the turbulent boundary layers and the channel flows. Only a few studies have investigated field line curvature and torsion directly and none in wall-turbulence. This is partly associated with the work being computationally intensive, and thus devising an efficient way to do the requisite computations is also non-trivial. The two main emphases of this research pertain to (*i*) the geometry of the mean dynamics, and (*ii*) the geometric properties of field lines. These are now discussed further.

2.2.1 Mean dynamical structure and its geometric implications

A central distinction between the classical versus MMB based descriptions (apart from the former having a direct basis in the RANS equations) pertains to the onset and scaling properties of the physical space *inertial sublayer* that is a primary focus in many experimental and theoretical studies [Klewicki, 2010, Marusic *et al.*, 2010]. The classical logarithmic layer is the lower part of fourth layer in the mean momentum balance where the viscous force (VF) is no longer leading

order. The clearest and most important evidences of scale separation phenomena in wall-flows are seen in the logarithmic layer. The leading balance layer structure has unambiguous connection with the relevant mean dynamics. In the classical description, one surmises that viscous effects become sub-dominant beginning at a distance that is $y = O(\nu/u_\tau)$ from the wall (typically around $y^+ = yu_\tau/\nu = 100$), where the friction velocity is defined by $u_\tau = \sqrt{\tau_w/\rho}$, with τ_w denoting the mean wall shear stress, and ν and ρ respectively denoting the kinematic viscosity and mass density. In the MMB based description, the loss of a leading order VF is found to occur at a wall-normal position $y \propto \sqrt{\nu\delta/u_\tau}$ or equivalently, $y^+ \propto \sqrt{\delta^+}$ (here, $\delta^+ = \delta u_\tau/\nu$), where δ in Table 1 denotes either the half-channel height or the boundary layer thickness. (Herein, the boundary layer δ is determined using the composite profile formulation of Chauhan *et al.* [2009]). This square root Reynolds number dependence ($\sqrt{\delta^+}$) is experimentally supported by measurements of the terms in the MMB, and analytically via multi-scale treatment of the MMB [Klewicki *et al.*, 2009, Morrill-Winter *et al.*, 2017*a*, Wei *et al.*, 2005]. This first appearance of inertially dominated flows is additionally supported by measurements of the logarithmic layer onset at high Reynolds number [Marusic *et al.*, 2013].

Analysis of the Reynolds Averaged Navier-Stokes (RANS) equations, as simplified for the canonical turbulent wall-flows reveals a layer structure associated with the leading order balances with distance from the wall [Morrill-Winter *et al.*, 2017*a*, Wei *et al.*, 2005]. The inner-normalized mean momentum equation for turbulent channel flow is given by the following equation,

$$0 = \frac{1}{\delta^+} + \frac{d^2U^+}{dy^{+2}} + \frac{dT^+}{dy^+} \tag{2.1}$$

0=PG(Pressure gradient)+VF(Viscous force)+TI(Turbulent inertia)

where, $T^+ = -<uv>/u_\tau^2 = -<uv>^+$ (superscript "+" means normalized quantity) is most often referred to as the Reynolds shear stress [Wei *et al.*, 2005]. For the flat plate boundary layer and fully developed channel (or pipe) flows, the mean momentum balance (MMB) equation 2.1 have these three terms. In the boundary layer, the three terms are mean inertia, turbulent inertia (gradient of the Reynolds shear stress), and the mean viscous force. These are respectively denoted MI, TI, and VF. For channel flow, the TI and VF terms are also present, but the MI term is replaced by the mean pressure gradient (PG). While in either case, all three terms are dominant order somewhere in the flow, not all are leading order everywhere. As described in Table 1, the layer structure (Viscous sublayer, Stress gradient balance layer, Meso layer, Inertial layer) associated with the leading balances in the MMB is qualitatively different from the classical viscous sublayer, buffer layer, logarithmic and wake layer description that derives from the observed features of the mean velocity profile [Klewicki, 2013*a*, Wei *et al.*, 2005].

Table 1. Inner normalized leading order balance layer thicknesses for boundary layer and channel flows.

Leading balance (channel)	**Leading balance (boundary layer)**	**Layer thickness (channel)**	**Layer thickness (boundary layer)**
I. $\|\mathrm{VF}\| \simeq \|\mathrm{MI}\|$	$\|\mathrm{VF}\| \simeq \|\mathrm{PG}\|$	$0 \leq y^+ \leq 4$	$0 \leq y^+ \leq 4$
II. $\|\mathrm{VF}\| \simeq \|\mathrm{TI}\|$	$\|\mathrm{VF}\| \simeq \|\mathrm{TI}\|$	$4 \leq y^+ \leq 1.6\sqrt{\delta^+}$	$4 \leq y^+ \leq 2.6\sqrt{\delta^+}$
III. $\|\mathrm{VF}\| \simeq \|\mathrm{TI}\| \simeq \|\mathrm{MI}\|$	$\|\mathrm{VF}\| \simeq \|\mathrm{TI}\| \simeq \|\mathrm{PG}\|$	$1.6\sqrt{\delta^+} \leq y^+ \leq 2.6\sqrt{\delta^+}$	$2.6\sqrt{\delta^+} \leq y^+ \leq 3.6\sqrt{\delta^+}$
IV. $\|\mathrm{TI}\| \simeq \|\mathrm{MI}\|$	$\|\mathrm{TI}\| \simeq \|\mathrm{PG}\|$	$2.6\sqrt{\delta^+} \leq y^+ \leq \delta^+$	$3.6\sqrt{\delta^+} \leq y^+ \leq \delta^+$

Fig. 2.1 shows a sketch of the leading balance layer structure of wall-bounded turbulent flows. For the channel, a balance between pressure gradient and viscous stress gradient is predominant in layer I, while the Reynolds stress gradient and viscous stress gradient balance in layer II. Layer III includes a balance among the three terms (the pressure gradient, viscous stress gradient and Reynolds stress gradient) of the momentum equation 2.1. Pressure gradient and Reynolds stress gradient balance each other in layer IV.

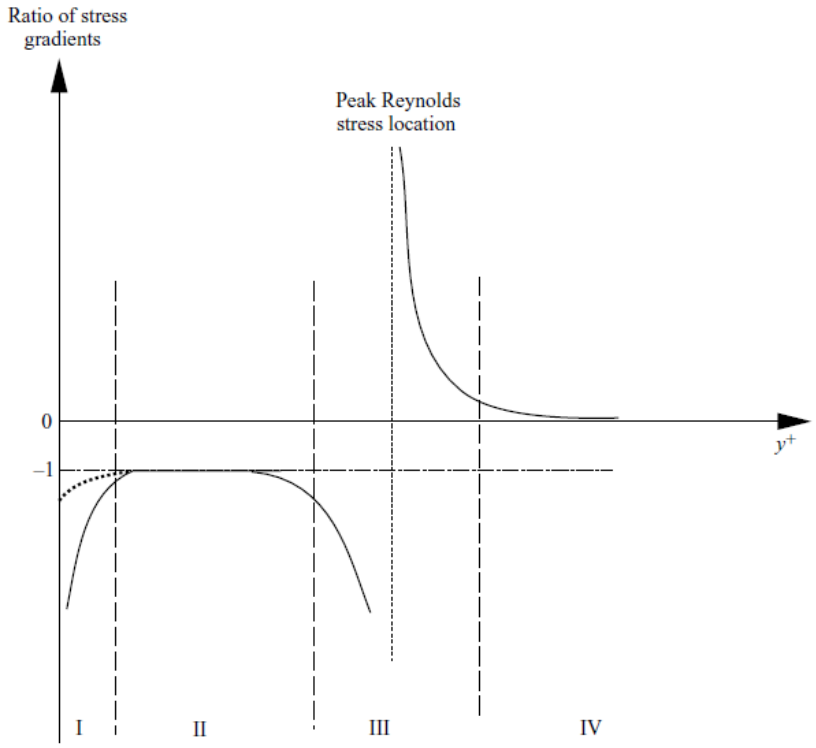

FIGURE 2.1: Four layer structure of wall-bounded turbulent flows from Wei *et al.* [2005]

The analysis of Fife *et al.* [2005] and Klewicki *et al.* [2014] indicates that the mean momentum balance (MMB) theory predicts that a self-similar geometric structure underlies the layer structure of Fig. 2.1. This consists of a continuous scaling layer hierarchy, where on each layer there is a balance exchange like across layer III that occurs as a function of scale with increasing y^+. Fig. 2.2 depicts a discrete representation of this layer hierarchy. Here, W is the width of each layer and β is a parameter that has a one to one correspondence with the wall-normal distance y^+. The relationship from one layer to the next is that y_2^+ is a distance that is W_1^+ from y_1^+ and so forth.

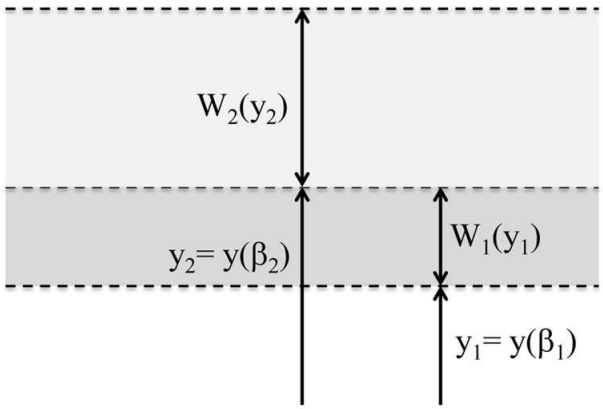

FIGURE 2.2: Schematic of the layer structure from Klewicki *et al.* [2014]

From an analysis of the structure of Fig. 2.2, Klewicki *et al.* [2014] show that the momentum transporting motions are self-similarly space-filling. The time fraction that the uv time series signal is described as a function of $y^+/\sqrt{\delta+}$ in Fig. 2.3. This time fraction is equivalent to its space fraction. Thus this statistics depicts the area coverage of the motions responsible for the wallward transport of momentum.

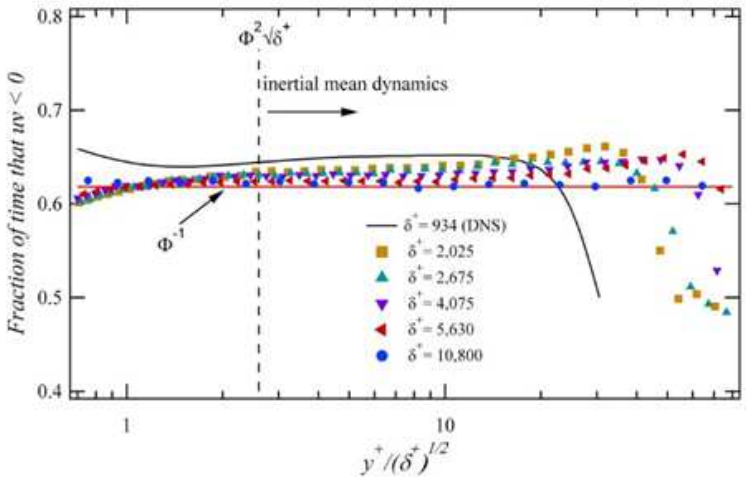

FIGURE 2.3: Area fraction that uv is negative for various δ^+ and plotted verses $y^+/\sqrt{\delta+}$ from [Klewicki *et al.*, 2014]

The present research aims to better understand the streamline geometry to better clarify the shape and the mechanisms of the dynamically important motions. In this regard, the streamline geometry statistics in the different layers of the boundary layer will be discussed in the result chapter. Furthermore, the inherent geometric self-similarity can be represented in terms of turbulent eddies that are the key topic of the next section.

2.2.2 Attached eddy hypothesis

Townsend's Attached Eddy Hypothesis [Townsend, 1976] also inherently leverages connections between geometry and kinematic structure of turbulent wall-flows. In this model, the mechanism of the wall-turbulence can be considered by representative attached eddies. The eddies are attached in the sense of this very well-known Townsend's attached eddy hypothesis (1976, page:153): "The velocity fields of the main (energy containing) eddies regarded as persistent, organized flow patterns extend to the wall and, in a sense they are attached to the wall". Perry & Chong [1982] proposed the hierarchy of geometrically similar eddies, that is shown in Fig. 2.4.

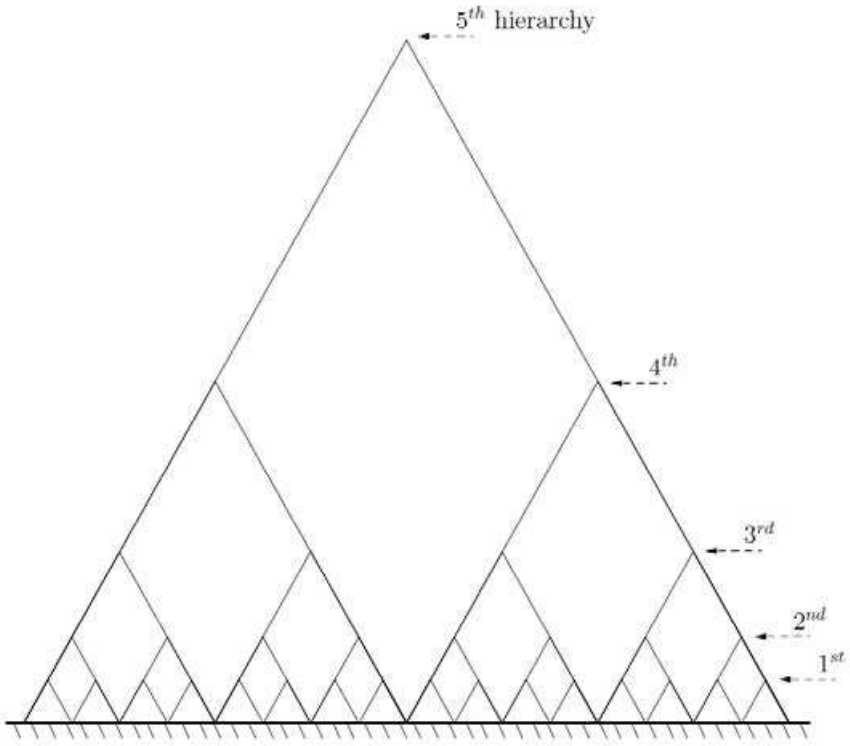

FIGURE 2.4: Symbolic representation of a discrete system of hierarchies

The maximum characteristic height of the largest eddies is proportional to the boundary layer thickness. The size of the eddies scale with their distance from the wall and velocity scales with friction velocity. The probability density function

(pdf) of eddies is inversely proportional to their distance from the wall. So, eddies are geometrically self-similar within the boundary layer. The attached eddy hypothesis is founded on the notion of the distance from the wall scaling that also comes out from the mean momentum balance theory. How these and other properties pertain to the curvature of the streamlines within the boundary layer flow are analysed briefly in the streamline studies section.

2.2.3 Mean momentum balance results

The present research seeks to inform the nature and origin of recently observed connections between this theory and the dynamics, and geometry of wall-turbulence. A primary focus of this research is to clarify recent empirical observations that the inertial region of wall turbulence exhibits self-similar behaviours, and that these behaviours are reflected in geometric properties associated with dynamically relevant quantities. Hence, the study is related to the flow behaviours within the self-similar inertial region unique to turbulent wall-flows. In this regard, Wei *et al.* [2005] have revealed dependency of mean structure of boundary layer, pipe and channel flows on Reynolds number in Fig. 2.1. This work has been extended by the theory of Fife *et al.* [2005]. In their work, they have clearly established the dependency behaviour of the mean momentum balance on the Reynolds number. Klewicki [2013*b*] and Klewicki *et al.* [2014] present some basic observations (figures 2.2 and 2.3). The first study has investigated the reason and results about the appearance of dynamical self-similarities in turbulent wall flows, and also has reported their behaviour with increasing Reynolds number. A part of this paper specifically relates to the von Kármán constant (k) and its connections to the solution of the mean dynamical equation. The second study discloses features of k that relate to the geometric structure of the flow. Vassilicos *et al.* studied the von Kármán constant (k) around the stagnation point and renamed as von Kármán coefficient (Dallas *et al.* [2009]) (discussed later). The self-similar spatial structure admitted by the MMB equations in that study [Klewicki *et al.*, 2014] is of inherent interest owing to its potential connection to the underlying geometry of the turbulence. A key finding here is that the mean equations formally admit an invariant form across a hierarchy of scaling layers. The widths of the members of this layer hierarchy span from $O(\nu/u_\tau)$ to $O(\delta)$, as do the locations of these layers. Importantly, the y coordinate stretching function (required to generate the invariant self-similar form of the MMB) becomes a linear function of distance from the wall on the inertial sublayer (i.e., beyond layer III) [Klewicki, 2013*a*]. This analytical result underpins the existence of a formally admitted similarity solution to the mean equations that is shown to recover the classical logarithmic mean velocity profile equation as $\delta^+ \to \infty$ [Klewicki & Oberlack, 2015, Morrill-Winter *et al.*, 2017*a*]. These and related analytical properties also support the existence of, and a number of evidence for, self-similar behaviours of the velocity field motions on the inertial sublayer [Meneveau & Marusic, 2013, Zhou & Klewicki, 2015]. In the present study, we similarly examine streamline curvature and torsion statistics in this context.

Physically, the widths of the layer hierarchy represent a characteristic scale of the motions responsible for wallward momentum transport, and this motivated more detailed analyses of the spatial structure of the negative Reynolds stress fluctuations. These investigations [Klewicki *et al.*, 2014, Morrill-Winter *et al.*, 2017*b*] revealed intriguing observations suggesting that the slope of the mean velocity profile on the inertial sublayer (as quantified by the von Kármán constant) relates to the space-filling properties of the negative Reynolds stress motions, and further that the amplitude and scale of these motions are self-similarly related. Alternatively, the inward flux of momentum can be equivalently viewed as being associated with the outward transport of vorticity [Eyink, 2008, Klewicki *et al.*, 2007]. In this regard, analyses in the context of the MMB reveal that near the wall the vorticity field is essentially space-filling and its dynamics are strongly coupled to the mechanisms of vorticity stretching and reorientation, which serve to rapidly three-dimensionalize the vorticity field. With increasing y, however, advection becomes the primary mechanism for vorticity transport, and is characterized by the spatial dispersion of small scale regions of intense vorticity [Morrill-Winter & Klewicki, 2013, Priyadarshana *et al.*, 2007]. In the present study, the mean curvature statistics reflect evidences of this feature of the vorticity stretching behaviour from the high turbulence region close the wall to the outer edge of layer II. With increasing y this behaviour is similarly shown to correlate with the decreasing density of stagnation points in the fluctuating velocity field (described relative to the studies of Vassilicos *et al.* [Dallas *et al.*, 2009, Goto & Vassilicos, 2009] below), as well as the statistical properties of the fluctuating streamline curvature documented herein.

2.2.4 Streamline studies

The present research aims to elucidate the origin of recent analyses and observations that point to compelling connections between the dynamics of the flow, and geometric properties of the turbulent motions responsible for these dynamics. Accordingly, this investigation includes exploring velocity and vorticity streamline curvature and torsion statistics in wall-turbulence. This involves the mathematics of differential geometry [Millman & Parker, 1977]. Previous researchers have studied the curvature geometry of turbulent flows for both streamlines [Peters *et al.*, 2010, Schaefer, 2012] and particle trajectories [Braun *et al.*, 2006, Scagliarini, 2011]. For particle trajectories, Braun *et al.* [2006], show that the maximum vorticity and the curvature of the particle trajectories are linearly correlated. Our present joint pdf on streamline curvature and torsion with velocity magnitude also reinforce this relationship in case of wall-bounded flows. Accordingly, Scagliarini [2011] studied the geometric properties of Lagrangian trajectories for homogeneous and isotropic turbulence. According to this study, the instantaneous curvature statistics are dominated by the large scales flow reversals, where the velocity magnitude assumes very low values. The joint statistics of curvature and torsion in his study highlight the coherent geometrical structure of small-scale intense vorticity in turbulent flows that are dominated by helical-type trajectories. For defining the turbulent structures at the small scales, the whole DNS flow field was decomposed

by Peters *et al.* [2010] into the planar geometrical unit they called dissipation element. According to them, the ensemble of grid cells from which the same pair of extremal points is reached determines a spatial region which is called a dissipation element. The spatial properties of the turbulent fields have been simply structured by streamline segment analysis by Wang [2010]. He defined a streamline segment as the part of streamline starting from each grid point bounded by two adjacent extremal points of the velocity magnitude. Thus, the boundary surface of streamline segments contains all local extreme points that are the ending points of the dissipation elements [Schaefer *et al.*, 2012]. These local extreme points also include stagnation points of the flow fields which are absolute minimum points of the turbulent kinetic energy as they described. Hence, the dissipation elements and the streamline segments are interrelated. In the present study, we have found that the stagnation points largely correlate with the larger curvature values. Given to this, the following discusses a particularly relevant study of Schaefer.

2.2.5 Most relevant streamline curvature literature

The most relevant work to the present study is the curvature statistics of streamlines in various turbulent flows studied by Schaefer Schaefer [2012]. He showed that the convective term of the Navier-Stokes equation can be expressed by the curvature related geometry of streamlines. In his study, he considered the curvature and torsion as a field variable in case of low Reynolds number isotropic flows. In contrast to this, the present work considers the curvature and torsion as a local variable and compute these in wall-bounded turbulent flow cases. Schaefer's research demonstrated that the probability density function of curvature $P(\kappa)$ follows a power-law scaling of κ^{-4} for the extreme curvature values, which as been suggested to around the stagnation points. This is reinforced by the present joint pdf of the curvature with fluctuating velocity magnitude result. Here, the exponent of -4 scaling derives from the following procedure as described by Schaefer Schaefer [2012]. The curvature is directly proportional to the product of the inverse of the velocity magnitude ($|V|^{-1}$) and the gradient of the velocity magnitude in the streamline direction. It is assumed that the pdfs of the two products are independent. Further, if the three velocity components is assumed to be joint Gaussian random variables, a scaling of the pdf of the inverse of absolute velocity value, $|V|^{-1} =: \mathfrak{a}$, can be found for isotropic turbulence. It can be then shown that the pdf of the turbulence kinetic energy $\mathfrak{K} = u_i u_i/2$ follows a chi square (χ^2) distribution with three degrees of freedom, which generates $P(\mathfrak{K}) \propto \mathfrak{K}^{1/2}\mathrm{e}^{-\mathfrak{K}/2}$. This gives, $P(\mathfrak{a}) \propto \mathfrak{a}^{-4}\mathrm{e}^{-\mathfrak{a}^{-2}}$. Following this, the pdf of the absolute value of curvature can be expressed κ^{-4}. The present curvature pdfs are analysed with respect to this exponent of -4 scaling that are discussed in the probability density function of curvature section.

Fig. 2.5 shows the normalized pdf of the Gaussian curvatures of streamlines of turbulent flows for four different DNS from Schaefer [2012]. Here, the probability density function of the Gaussian curvature is normalized by its standard deviation. The algebraic tails of the pdf scale as $\tilde{\kappa}_g^{-4}$ corresponds very large value of curvature.

Where and why similar behaviours exist in wall turbulence is one of the important elements of the present study. Thus, the present wall-flow research constitutes a natural extension to his work, and thus worthy of deeper inquiry.

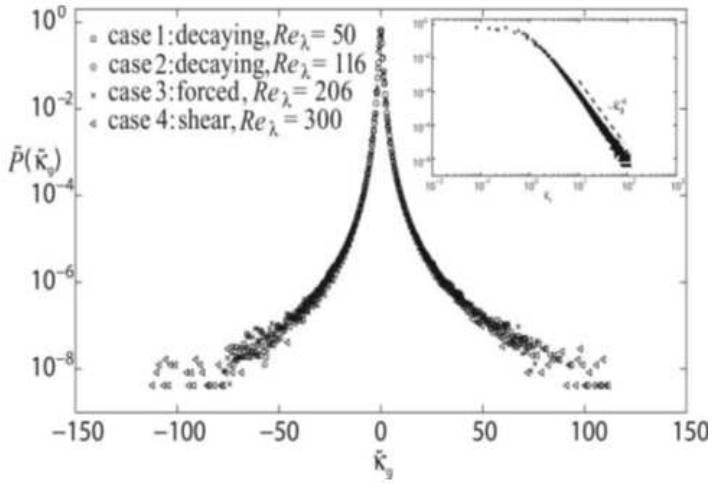

FIGURE 2.5: Normalised pdf of the Gaussian curvature of streamlines from Schaefer [2012]

The above discussions motive the study of geometric aspects of the flow. The narrative below provides additional details from the existing literature.

2.2.6 Stagnation point structure in turbulent wall-flows

Motivated by earlier investigations of the zero-crossing properties of velocity fluctuations and their derivatives [Mazellier & Vassilicos, 2008, Sreenivasan *et al.*, 1983], Vassilicos and co-workers studied the properties of the zeros (stagnation points) of the fluctuating velocity magnitude in turbulent channel flows [Dallas *et al.*, 2009, Goto & Vassilicos, 2009]. Stagnation points are defined as the points where the fluctuating velocity components around the local mean flow are zero [Dallas *et al.*, 2009]. For the fluctuating velocity fields, Dallas *et al.* [Dallas *et al.*, 2009] found that the distance between stagnation points is proportional to the Taylor microscale. In the region where the mean velocity profile is logarithmic (i.e., inertial sublayer- inner part of layer IV in Table 1), they also showed that the number density of the stagnation points is inversely proportional to the wall-normal distance. In the present study, we explore the onset of -4 scaling (related to extreme curvature values near stagnation points) with the inverse of Kolmogorov scale, and the ratio of the Taylor microscale to the radius of curvature with wall-normal distances.

2.3 Connection between geometry and dynamics of wall-flows

The present research is based on the idea that there are spatial signatures related to the shape and the mechanisms of the motions that affect the flow dynamics. Our interest is to identify the connection of this spatial geometry to the flow dynamics. There are good reasons that lead one to suspect that such relations exist. For example recent research (say over the past 30 years i.e. [Klewicki *et al.*, 2014], [Schaefer, 2012], [Braun *et al.*, 2006]) indicates the importance of coherent vortical motions in turbulent flows, and that these motions are spatially organized. These coherent regions of vorticity are generally known as "turbulent eddies". Turbulent eddies will generally have non-zero streamline curvature. So, from the properties of the local curvature through the entire flow field, it is hypothesized that we can learn more about the coherent vortical motions in wall-flows. An order of magnitude analysis of leading terms in the mean momentum balance indicates dynamically distinct regions within the boundary layer and an associated geometric structure. Overall, the geometric properties of wall-bounded flows have not yet been studied in detail. Worthy areas of exploration thus includes two broad themes; (*i*) The properties of the inertial turbulent motions that underlie the self-similar geometric structure found through analysis of the mean momentum balance, and (*ii*) The geometric properties of the velocity and vorticity field lines and their correlation to dynamical structure. The present study focuses on the latter.

Chapter 3

Calculation technique and code validation

In this study, the streamlines are computed at each grid point of a flow field to calculate the local curvature and torsion. The curvature and torsion equations are derived from the Frenet-Serret apparatus. The Runge-Kutta method is used for point-wise streamlines calculations. For validation, in the last section of this chapter we compare the curvature and torsion values using the present calculation method with the known results in the case of a straight line, circle, and helix.

3.1 Curvature and torsion calculation methods

This section includes the calculation technique for curvature and torsion. Curvature is calculated using two methods. The first uses the central difference formula for the equation of curvature as derived from the Frenet-Serret apparatus. The second uses the magnitude of the vector formula for the curvature components.

3.1.1 Frenet-Serret apparatus

Pragmatically, the interrogation of field line curvature and torsion in DNS data sets effectively involves the computational construction of the local Frenet-Serret apparatus. The Frenet-Serret apparatus is an orthogonal coordinate system defined locally along a space curve and is used herein as a basis for computing the local geometry of the streamlines [Millman & Parker, 1977]. This tool relates the three basic vectors of differential geometry; the tangent vector $\mathbf{T}$, normal vector $\mathbf{N}$ and binormal vector $\mathbf{B}$; as well as two scalar quantities: curvature κ and torsion τ. Here, $\mathbf{T}$ is a unit vector pointing in the direction of the velocity vector, $\mathbf{N}$ is a unit vector pointing along the radius of curvature (outward) and $\mathbf{B}$ is the unit vector that is orthogonal to both $\mathbf{T}$ and $\mathbf{N}$. The scalar quantity, curvature quantifies the bending of a curve from a straight line within a reference plane. Thus, for example,

the curvature value for a straight line is zero, and that of a circle of radius r is constant and equal to $1/r$. Torsion measures the out-of-plane motion of a curve, i.e. the twisting motion of the curve. Fig. 3.1 shows the local coordinate system with the tangent, normal and binormal vector in case of a right-handed helix.

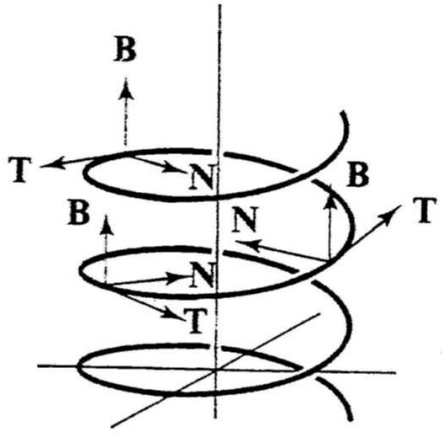

FIGURE 3.1: Frenet-Serret apparatus shown by Millman & Parker [1977]

The Frenet-Serret equations for a unit speed curve $\boldsymbol{\alpha}(s)$, relations between $\mathbf{T}, \mathbf{N}, \mathbf{B}, \kappa$ and τ and are given by,

$$\mathbf{T}' = \kappa \mathbf{N}, \tag{3.1}$$

$$\mathbf{N}' = -\kappa \mathbf{T} + \tau \mathbf{B}, \tag{3.2}$$

$$\mathbf{B}' = -\tau \mathbf{N}. \tag{3.3}$$

Here, the superscript prime denotes the first derivative with respect to speed parameter, s, which is the variable that moves one along the curve as it is traced out in space. Here, s is a length scale that is defined as the speed parameter in accordance with the nomenclature of differential geometry.

Now, let a streamline at any fixed instant in the flow evolution be defined by $\boldsymbol{\beta}$. The curve $\boldsymbol{\beta}$ will be equivalent to $\boldsymbol{\alpha}(s)$ if it is parametrized by the arc length. Thus, $\boldsymbol{\beta}$ is a function of s. $\dot{\boldsymbol{\beta}}$ represents the first derivative of the curve with respect to the speed at which one travels along the curve. If the curve is fixed in space (as are streamlines at any instant of flow evolution) then the pseudo-time derivative along this fixed curve refers to moving at a uniform speed along that curve. Computationally this means that discrete calculations must use equally spaced data points along the curve. The derivatives of $\boldsymbol{\beta}$ are then unambiguously related to the shape of the curve.

Thus if we talk about the travel of a particle moving along this fixed space curve then its pseudo time derivative (e.g. $\dot{\boldsymbol{\beta}}$) is related to the local geometric properties of the curve. Note that this pseudo-time is not associated with the flow evolution, but rather the trajectory along a fixed space curve. If the pseudo-time

is normalized by arc length, then the pseudo-time derivative of a uniform speed curve is equivalent to the derivative of the unit speed curve using the arc length. Once again, the pseudo-time is considered for each fixed time instant in the flow field evolution. Overall the procedure used herein is equivalent to that used by Schaefer [2012].

Following the above prescription, the equation for the tangent of the streamline ($\boldsymbol{\beta}$) is then given by

$$\mathbf{T} = \frac{\dot{\boldsymbol{\beta}}}{|\dot{\boldsymbol{\beta}}|}, \tag{3.4}$$

or

$$\dot{\boldsymbol{\beta}} = |\dot{\boldsymbol{\beta}}|\mathbf{T},$$

where $\dot{\boldsymbol{\beta}}$ is the pseudo-time derivative of $\boldsymbol{\beta}$. The second derivative of $\boldsymbol{\beta}$ implies,

$$\ddot{\boldsymbol{\beta}} = |\ddot{\boldsymbol{\beta}}|\mathbf{T} + |\dot{\boldsymbol{\beta}}|\dot{\mathbf{T}}. \tag{3.5}$$

Using the re-parameterization $\dot{\mathbf{T}} = |\dot{\boldsymbol{\beta}}|\mathbf{T}'$ and equation (3.1),

$$\ddot{\boldsymbol{\beta}} = |\ddot{\boldsymbol{\beta}}|\mathbf{T} + |\dot{\boldsymbol{\beta}}||\dot{\boldsymbol{\beta}}|\mathbf{T}'.$$

Or,

$$\ddot{\boldsymbol{\beta}} = |\ddot{\boldsymbol{\beta}}|\mathbf{T} + |\dot{\boldsymbol{\beta}}||\dot{\boldsymbol{\beta}}|\kappa\mathbf{N},$$

and thus,

$$\ddot{\boldsymbol{\beta}} = |\ddot{\boldsymbol{\beta}}|\mathbf{T} + |\dot{\boldsymbol{\beta}}|^2\kappa\mathbf{N}\ . \tag{3.6}$$

Here, $\dot{\boldsymbol{\beta}}$ and $\ddot{\boldsymbol{\beta}}$ are respectively defined as velocity and acceleration of a particle moving along the streamline $\boldsymbol{\beta}$ curve. The cross product of the velocity and acceleration gives,

$$\dot{\boldsymbol{\beta}} \times \ddot{\boldsymbol{\beta}} = |\dot{\boldsymbol{\beta}}|\mathbf{T} \times (|\ddot{\boldsymbol{\beta}}|\mathbf{T} + |\dot{\boldsymbol{\beta}}|^2\kappa\ \mathbf{N}) = |\dot{\boldsymbol{\beta}}|^3\kappa\mathbf{B}, \tag{3.7}$$

as $\mathbf{T} \times \mathbf{T} = 0, \mathbf{T} \times \mathbf{N} = \mathbf{B}$ [using right-handed rule]. The magnitude of the unit vector $\mathbf{B}$ is one. Thus,

$$\kappa = \frac{|\dot{\boldsymbol{\beta}} \times \ddot{\boldsymbol{\beta}}|}{|\dot{\boldsymbol{\beta}}|^3}. \tag{3.8}$$

Now, for the calculation of torsion, we start with the derivative of equation 3.6,

$$\dddot{\boldsymbol{\beta}} = |\dddot{\boldsymbol{\beta}}|\mathbf{T} + |\ddot{\boldsymbol{\beta}}|\dot{T} + \kappa\mathbf{N}\ (|\dot{\boldsymbol{\beta}}|^2)^{\cdot} + \kappa|\dot{\boldsymbol{\beta}}|^2\dot{\mathbf{N}}\ . \tag{3.9}$$

Using the re-parameterizations, $\dot{\mathbf{N}} = |\dot{\boldsymbol{\beta}}|\mathbf{N}'$ and $\dot{\mathbf{T}} = |\dot{\boldsymbol{\beta}}|\mathbf{T}'$,

$$\dddot{\boldsymbol{\beta}} = |\dddot{\boldsymbol{\beta}}|\mathbf{T} + |\ddot{\boldsymbol{\beta}}||\dot{\boldsymbol{\beta}}|\mathbf{T}' + \kappa\mathbf{N}\ (|\dot{\boldsymbol{\beta}}|^2)^{\cdot} + \kappa|\dot{\boldsymbol{\beta}}|^2|\dot{\boldsymbol{\beta}}|\mathbf{N}'.$$

Using equations 3.1 and 3.2

$$\begin{aligned}\dddot{\boldsymbol{\beta}} &= |\dddot{\boldsymbol{\beta}}|\mathbf{T} + |\ddot{\boldsymbol{\beta}}||\dot{\boldsymbol{\beta}}|\kappa\mathbf{N} + \kappa\mathbf{N}\ (|\dot{\boldsymbol{\beta}}|^2)^{\cdot} + \kappa|\dot{\boldsymbol{\beta}}|^3(-\kappa\mathbf{T} + \tau\mathbf{B}) \\ &= |\dddot{\boldsymbol{\beta}}|\mathbf{T} - \kappa^2|\dot{\boldsymbol{\beta}}|^3\mathbf{T} + |\dot{\boldsymbol{\beta}}||\ddot{\boldsymbol{\beta}}|\kappa\mathbf{N} + \kappa\mathbf{N}\ (|\dot{\boldsymbol{\beta}}|^2)^{\cdot} + \kappa\tau|\dot{\boldsymbol{\beta}}|^3\mathbf{B},\end{aligned}$$

and thus

$$\dddot{\boldsymbol{\beta}} = (|\dddot{\boldsymbol{\beta}}| - \kappa^2|\dot{\boldsymbol{\beta}}|^3)\mathbf{T} + (|\dot{\boldsymbol{\beta}}||\ddot{\boldsymbol{\beta}}|\kappa + \kappa(|\dot{\boldsymbol{\beta}}|^2)^{\cdot})\mathbf{N} + \kappa\tau|\dot{\boldsymbol{\beta}}|^3\mathbf{B}. \tag{3.10}$$

Here, $[\dot{\boldsymbol{\beta}}, \ddot{\boldsymbol{\beta}}, \dddot{\boldsymbol{\beta}}] = (\dot{\boldsymbol{\beta}} \times \ddot{\boldsymbol{\beta}}).(\dddot{\boldsymbol{\beta}}) = \langle(\dot{\boldsymbol{\beta}} \times \ddot{\boldsymbol{\beta}}), \dddot{\boldsymbol{\beta}}\rangle$. In the middle term, by using equation 3.7 and 3.10 we get,

$$(\dot{\boldsymbol{\beta}} \times \ddot{\boldsymbol{\beta}}).(\dddot{\boldsymbol{\beta}}) = [|\dot{\boldsymbol{\beta}}|^3\kappa\mathbf{B}].[(|\dddot{\boldsymbol{\beta}}| - \kappa^2|\dot{\boldsymbol{\beta}}|^3)\mathbf{T} + (|\dot{\boldsymbol{\beta}}||\ddot{\boldsymbol{\beta}}|\kappa + \kappa(|\dot{\boldsymbol{\beta}}|^2)^{\cdot})\mathbf{N} + \kappa\tau|\dot{\boldsymbol{\beta}}|^3\mathbf{B}],$$

and thus, $(\dot{\boldsymbol{\beta}} \times \ddot{\boldsymbol{\beta}}).\dddot{\boldsymbol{\beta}} = \kappa^2\tau|\dot{\boldsymbol{\beta}}|^6$, (using $\mathbf{B}.\mathbf{T} = 0, \mathbf{B}.\mathbf{N} = 0, \mathbf{B}.\mathbf{B} = 1$)

or, $(\dot{\boldsymbol{\beta}} \times \ddot{\boldsymbol{\beta}}).\dddot{\boldsymbol{\beta}} = \tau(\kappa|\dot{\boldsymbol{\beta}}|^3)^2$.

Or, $(\dot{\boldsymbol{\beta}} \times \ddot{\boldsymbol{\beta}}).(\dddot{\boldsymbol{\beta}}) = \tau|\dot{\boldsymbol{\beta}} \times \ddot{\boldsymbol{\beta}}|^2$ (Using equation 3.8)

yielding,

$$\tau = \frac{(\dot{\boldsymbol{\beta}} \times \ddot{\boldsymbol{\beta}}).\dddot{\boldsymbol{\beta}}}{|\dot{\boldsymbol{\beta}} \times \ddot{\boldsymbol{\beta}}|^2}, \tag{3.11}$$

and finally

$$\tau = \frac{[\dot{\boldsymbol{\beta}}, \ddot{\boldsymbol{\beta}}, \dddot{\boldsymbol{\beta}}]}{|\dot{\boldsymbol{\beta}} \times \ddot{\boldsymbol{\beta}}|^2}. \tag{3.12}$$

The derivatives of $\boldsymbol{\beta}$ in equations 3.8 and 3.12 are computed using the following **standard central difference formulas**;

$$\dot{\mathbf{B}}_j^n = \frac{\mathbf{B}_j^{n+1} - \mathbf{B}_j^{n-1}}{2\triangle t}, \tag{3.13}$$

where $\dot{\mathbf{B}}^n$ is the first derivative at the current (pseudo) time step, $\mathbf{B}^n$ is the location on the curve at the current time step, $\mathbf{B}^{n+1}$ is the location at the next time step, $\mathbf{B}^{n-1}$ is the location at the previous time step, $\triangle t$ is the change in the time and j denotes i, j or k.

The second and third derivatives are,

$$\ddot{\mathbf{B}}_j^n = \frac{\mathbf{B}_j^{n+2} - 2\mathbf{B}^n + \mathbf{B}_j^{n-2}}{4\triangle t^2}, \tag{3.14}$$

and

$$\dddot{\mathbf{B}}_j^n = \frac{\mathbf{B}_j^{n+3} - 3\mathbf{B}_j^{n+1} + 3\mathbf{B}_j^{n-1} - \mathbf{B}_j^{n-3}}{8\triangle t^3}. \tag{3.15}$$

3.1.2 Vector method for calculating curvature component

From differential geometry, the curvature is also defined by,

$$\kappa = \frac{d\mathbf{t}}{ds}, \tag{3.16}$$

where $d\mathbf{t}$ is the differential increment of the tangent vector and ds is the differential arc length of the curve. If the velocity components at a point on the streamline are defined by u_1, v_1, and w_1 then the total velocity is,

$$\mathbf{V} = u_1\hat{i} + v_1\hat{j} + w_1\hat{k}, \tag{3.17}$$

and the magnitude of $\mathbf{V}$ is

$$|\mathbf{V}| = |\sqrt{u_1^2 + v_1^2 + w_1^2}|. \tag{3.18}$$

Thus, the unit tangent vectors are,

$$\hat{t} = \frac{\mathbf{V}}{|\mathbf{V}|} = \frac{u_1}{|\mathbf{V}\ |}\hat{i} + \frac{v_1}{|\mathbf{V}|}\hat{j} + \frac{w_1}{|\mathbf{V}|}\hat{k} = t_{x1}\hat{i} + t_{y1}\hat{j} + t_{z1}\hat{k}. \tag{3.19}$$

Similarly, the unit tangent vector components t_{x2}, t_{y2}, and t_{z2} for the next point are computed to find $d\mathbf{t}_x, d\mathbf{t}_y, d\mathbf{t}_z$. The differential arc length ds is calculated by taking the distance between the first two points on the streamline. Then,

$$\kappa_x = \frac{dt_x}{ds},$$
$$\kappa_y = \frac{dt_y}{ds},$$

and

$$\kappa_z = \frac{dt_z}{ds} \tag{3.20}$$

are the curvature components in the streamwise, wall-normal and spanwise directions. Therefore the magnitude of the total curvature is,

$$\kappa = |\sqrt{\kappa_x^2 + \kappa_y^2 + \kappa_z^2}|. \tag{3.21}$$

Equations 3.8 and 3.21 are shown in Appendix A to yield the same computed curvature values.

3.2 Runge-Kutta method for calculating streamline

We use a 4th order Runge-Kutta method to compute the streamline starting at each grid point of a DNS flow volume. Here, the 3rd derivative is the highest derivative in the curvature and torsion definitions (equation 3.8 and 3.12), which requires a maximum seven points to execute the central difference formula in equation 3.15. Herein, we use the Runge-Kutta method to calculate a portion of the streamline, i.e. a streamline segment. The details procedure are shown in Appendix. The technique for choosing the step size that defines the space between two consecutive points on the streamline segment are discussed below.

3.2.1 The technique for choosing the step size

This section is about the computation of the step size h. The step size should not be taken too small or too large for numerical accuracy. Here, we consider 100 random values between .000001 and 100 on a logarithmic scale. We examine the mean, standard deviation, skewness and kurtosis of curvature for these random values of h. The idea here is to nominally determine the largest step such that the statistics at the surrounding points remain unchanged as shown in figure 3.2.

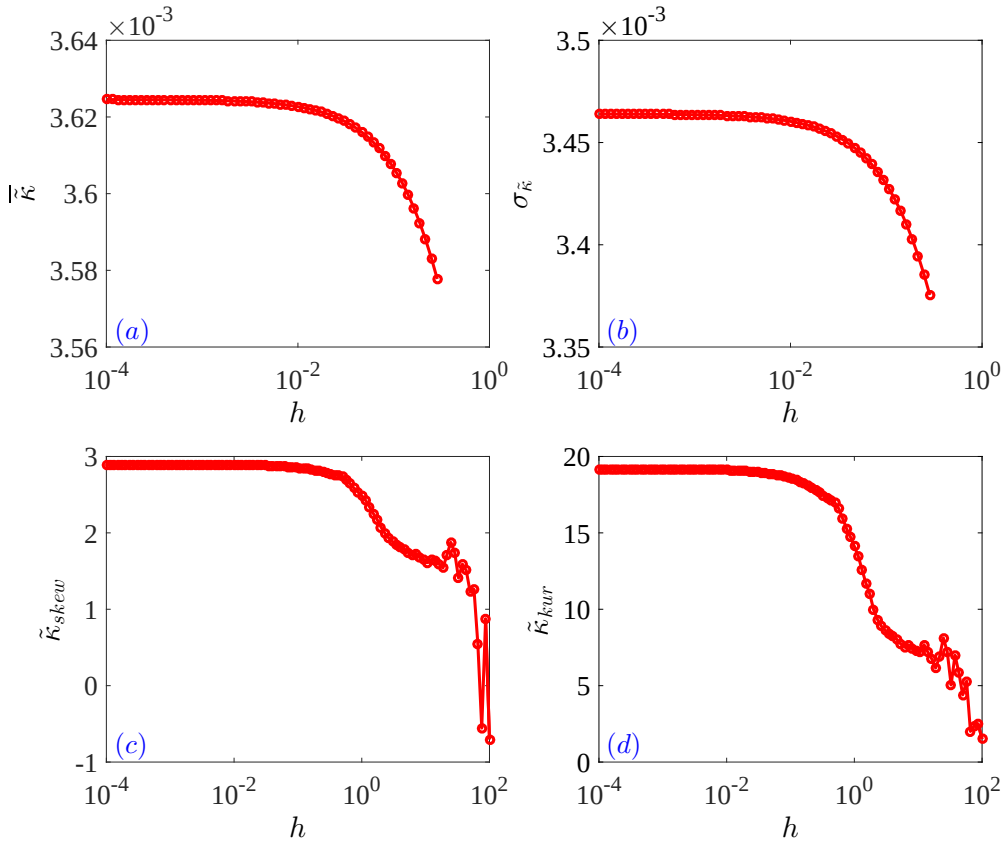

FIGURE 3.2: Curvature statistics versus step size h **(a)** mean curvature, **(b)** standard deviation, **(c)** skewness, and **(d)** kurtosis

Here, these statistics are defined as;

mean: $\overline{\kappa} = \sum \kappa_i / N$,

standard deviation: $\sigma_\kappa = \sqrt{\sum (\kappa_i - \overline{\kappa})^2 / N}$,

skewness: $\kappa_{skew} = \sum \frac{(\kappa_i - \overline{\kappa})^3 / N}{\sigma_\kappa^3}$, and

kurtosis: $\kappa_{kur} = \sum \frac{(\kappa_i - \overline{\kappa})^4 / N}{\sigma_\kappa^4}$,

where N is the size of the curvature ensemble. All plots of figure 3.2 show the statistical results remain constant up to $h \approx 10^{-3}$. After that, the profiles start decreasing. Thus we choose the step size $h = 0.001$ for this research, which is 0.14 in viscous unit.

3.3 Direct numerical simulation (DNS)

A direct numerical simulation (DNS) is a complete three-dimensional and time-dependent realization of the Navier-Stokes and continuity equations. The value of DNS is that it is potentially a numerically accurate solution of the exact equations of motion. This is especially useful for obtaining information about essentially unmeasurable properties like pressure fluctuations. DNS is free from the significant numerical and other forms of error. The primary concerns in DNS are related to numerical accuracy specification of initial and boundary conditions and making optimum use of available computer resources.

The present analysis employs DNS data sets. These include boundary layer data at friction Reynolds numbers $\delta^+ \approx 1310$ and $\delta^+ \approx 2000$ [Sillero *et al.*, 2013]), and channel flow data at friction Reynolds number $\delta^+ \approx 934$ [Del Alamo *et al.*, 2004]. The friction Reynolds number is defined as (also defined in Chapter 2), $\delta^+ = \delta u_\tau / \nu = Re_\tau$, where $u_\tau = \sqrt{\tau_w / \rho}$, ν is the kinematic viscosity, and δ denotes either the half-channel height or the boundary layer thickness. Here, in the case of the boundary layer, δ^+ was found to be about 1660 and 2530 using the composite profile formulation by [Chauhan *et al.*, 2009]. The streamwise, spanwise and the wall-normal directions are considered to be along the x-axis, z-axis, and y-axis respectively. For the channel flow, it is feasible to compute statistics over the entire plane owing to its horizontally homogeneous fully developed properties. The boundary layers, however, required the use of smaller domains to approximate a constant friction velocity condition. For this reason, the slices of only 312 grid points are considered in the x-direction and 2048 grid points are taken in the z-direction at 38 wall positions for $\delta^+ = 2530$ boundary layer (and similarly 195 and 4096 grid points in x and z respectively at 36 wall-positions in case of $\delta^+ = 1660$ boundary layer). For comparison, 312 and 2048 grid points are considered in x and z respectively at 37 wall-positions for $\delta^+ = 934$ channel DNS as well. Statistics are computed from the average of six independent DNS fields by averaging over the planar domains indicated above.

3.4 Code validation

The Matlab code for the curvature and torsion calculation is tested by the known results for straight line, circle, and helix. The curvature and torsion of a straight line are analytically known to be zero (not shown here). For a planar circle, the curvature is analytically equal to the inverse of the radius of the circle, and the torsion is zero as there is no out of plane motion. We have computed the curvature value for a straight line $\mathbf{S}(t) = (t, 0, 0)$ and for a circle $\mathbf{C}(t) = (rcos(t), rsin(t), 0)$ of radius $r = 5$ using the 4th order Runge-Kutta method with the curvature definition in equation 3.8. Here, we get the expected curvature values e.g. 0 and 0.2 for the considered straight line and circle respectively that are shown in figure 3.3.

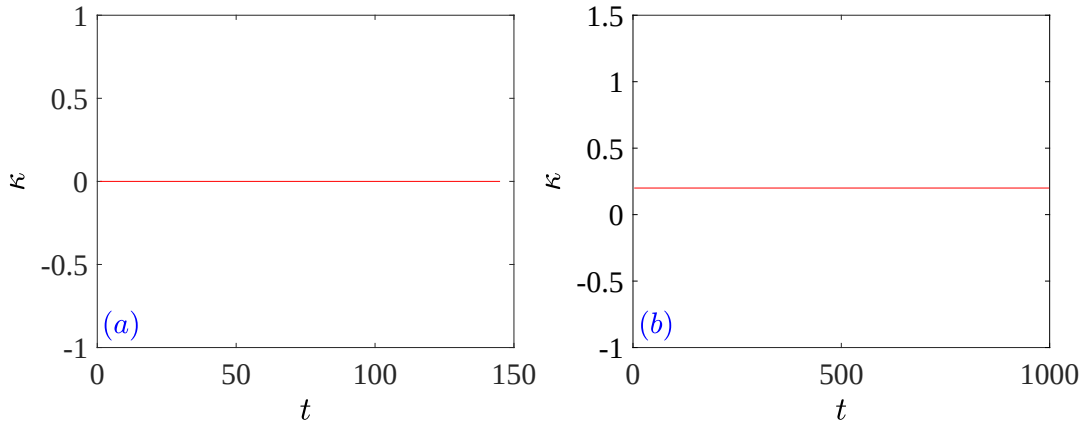

FIGURE 3.3: Curvature values for the considered **(a)** straight line **(b)** circle

3.4.1 Analytical solution for curvature and torsion in case of a helix

Let, a helix

$$\boldsymbol{\beta}(t) = (rcos(t), rsin(t), bt) \tag{3.22}$$

with radius $r = 1$ and pitch $2\pi b = 1$ (that returns $b = 0.1592$) which is shown in figure 3.4.

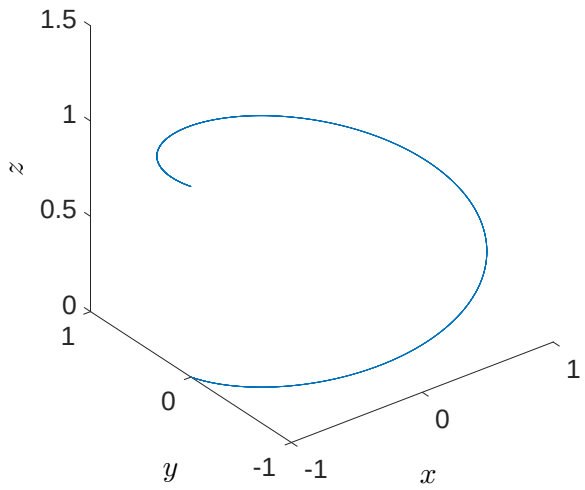

FIGURE 3.4: Unit helix with radius one and pitch one

Now, we will calculate the curvature and torsion for this helix using central difference formulas and vector method discussed in the first section of this chapter.

3.4.1.1 Finite (central) difference method

The curvature from equation 3.8 is

$\kappa = \frac{|\dot{\boldsymbol{\beta}} \times \ddot{\boldsymbol{\beta}}|}{|\dot{\boldsymbol{\beta}}|^3}$.

Here, using equation 3.22,

$\dot{\boldsymbol{\beta}} = (-rsin(t), rcos(t), b)$ and

$\ddot{\boldsymbol{\beta}} = (-rcos(t), -rsin(t), 0)$.

Therefore, $\dot{\boldsymbol{\beta}} \times \ddot{\boldsymbol{\beta}} = brsin(t)\hat{i} - brcos(t)\hat{j} + r^2\hat{k}$ and the magnitude

$|\dot{\boldsymbol{\beta}} \times \ddot{\boldsymbol{\beta}}| = \sqrt{(b^2r^2sin^2(t) + b^2r^2cos^2(t) + r^4)} = r\sqrt{(b^2 + r^2)}$ and

$|\dot{\boldsymbol{\beta}}| = \sqrt{(r^2sin^2(t) + r^2cos^2(t) + b^2)} = \sqrt{(b^2 + r^2)}$.

Thus,

$$\kappa = \frac{r\sqrt{(b^2 + r^2)}}{(\sqrt{(b^2 + r^2)})^3} = \frac{r}{(r^2 + b^2)}. \tag{3.23}$$

The torsion from equation 3.11 is

$$\tau = \frac{(\dot{\boldsymbol{\beta}} \times \ddot{\boldsymbol{\beta}}).\dddot{\boldsymbol{\beta}}}{|\dot{\boldsymbol{\beta}} \times \ddot{\boldsymbol{\beta}}|^2}. \tag{3.24}$$

Here, $\dddot{\boldsymbol{\beta}} = (rsin(t), -rcos(t), 0)$, thus,

$(\dot{\boldsymbol{\beta}} \times \ddot{\boldsymbol{\beta}}).\dddot{\boldsymbol{\beta}} = (brsin(t)\hat{i} - brcos(t)\hat{j} + r^2\hat{k}).(rsin(t)\hat{i} - rcos(t)\hat{j} + 0\hat{k})$

$= br^2sin^2(t) + br^2cos^2(t) + 0 = br^2.$

Therefore,

$$\tau = \frac{br^2}{(r\sqrt{b^2+r^2})^2} = \frac{b}{(b^2+r^2)}. \tag{3.25}$$

3.4.1.2 Vector method

The velocity at a point on the considered helix $\boldsymbol{\beta}(t) = (rcos(t), rsin(t), bt)$ with $u_1 = dx/dt = -rsin(t), v_1 = dy/dt = rcos(t), w_1 = dz/dt = b$, are

$|\mathbf{V}| = |d\boldsymbol{\beta}/dt| = \sqrt{(r^2sin^2(t) + r^2cos^2(t) + b^2)} = \sqrt{(r^2+b^2)}.$

The arc length is $s = \int_0^t |d\boldsymbol{\beta}/dt|dt = \int_0^t \sqrt{(r^2+b^2)}dt = t\sqrt{(r^2+b^2)}.$

From this, $t = \frac{s}{\sqrt{(r^2+b^2)}}$.

The tangent vectors are,

$t_{x1} = \frac{u_1}{|\mathbf{V}|} = \frac{-rsin(t)}{\sqrt{(r^2+b^2)}},$

$t_{y1} = \frac{v_1}{|\mathbf{V}|} = \frac{rcos(t)}{\sqrt{(r^2+b^2)}},$

$t_{z1} = \frac{w_1}{|\mathbf{V}|} = \frac{b}{\sqrt{(r^2+b^2)}}.$

Therefore the components of curvature are,

$\kappa_x = \frac{dt_x1}{ds} = \frac{d}{ds}(\frac{-rsin(t)}{\sqrt{(r^2+b^2)}}) = \frac{1}{\sqrt{(r^2+b^2)}}\frac{d}{ds}(-rsin(\frac{s}{\sqrt{(r^2+b^2)}})) = \frac{-r}{(r^2+b^2)}cos(\frac{s}{\sqrt{(r^2+b^2)}}),$

$\kappa_y = \frac{dt_y1}{ds} = \frac{d}{ds}(\frac{rcos(t)}{\sqrt{(r^2+b^2)}}) = \frac{1}{\sqrt{(r^2+b^2)}}\frac{d}{ds}(rcos(\frac{s}{\sqrt{(r^2+b^2)}})) = \frac{-r}{(r^2+b^2)}sin(\frac{s}{\sqrt{(r^2+b^2)}}),$

$\kappa_z = \frac{dt_z1}{ds} = \frac{d}{ds}\frac{b}{\sqrt{r^2+b^2}} = 0.$

Thus the curvature magnitude is,

$$\kappa = |\sqrt{\kappa_x^2 + \kappa_y^2 + \kappa_z^2}| = \frac{r}{(r^2+b^2)}. \tag{3.26}$$

Thus, equations 3.23 and 3.26 yield the same curvature value. This simplification of the considered helix for curvature and torsion using equations 3.8 and 3.12 gives, $\kappa = r/(r^2+b^2)$ and $\tau = b/(r^2+b^2)$. Therefore, analytically, the curvature and torsion values for this helix are 0.975295 and 0.155223 (using $r = 1, b = 0.1592$). Figure 3.5 shows the local curvature and torsion values computed using the present

calculation method for the considered helix. These results are exactly equal to the analytical values. Thus, all the results of this section support the validation of the calculation technique for this research.

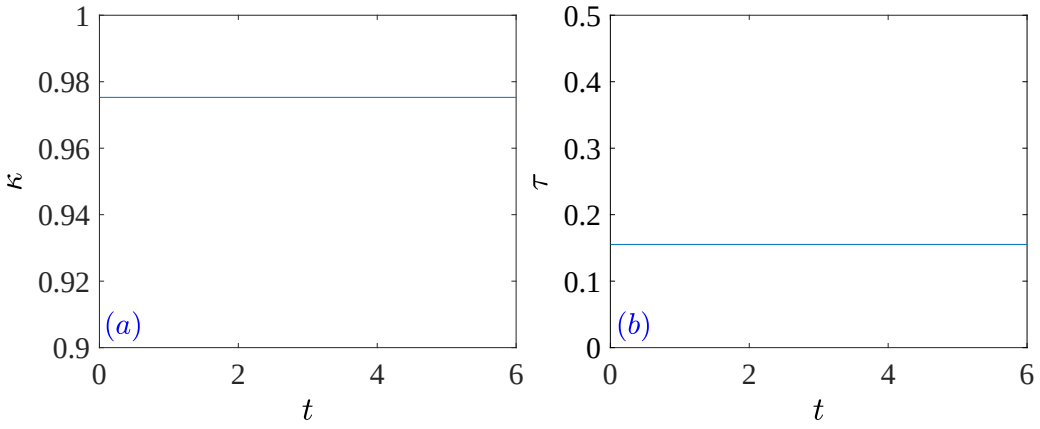

FIGURE 3.5: **(a)** Local curvature of the considered helix **(b)** Local torsion of the considered helix in figure 3.4

Chapter 4

Statistical properties of curvature and torsion

This chapter includes the curvature and torsion statistics for the considered wall-bounded flow cases. The analysis shows that the statistics of these geometrical properties change significantly with wall-normal position. Moreover, the correlation coefficient and the conditional average of the wall-normal velocity corresponding to the wall-normal curvature have been computed. The probability density function of the curvatures have been calculated at selected wall-normal locations and compared with a scaling of -4 for both total and fluctuating field. The pdf profile of the positive and negative wall-normal curvature shows a clear wall-blocking effect. The standard deviation for torsion, and the ratio of torsion and curvature have been shown for the analysis of the out of plane motion of streamlines. The joint pdf of curvature with velocity magnitude quantifies curvature values near stagnation points. Furthermore, the joint pdf of curvature components have been calculated to interpret the orientation of the streamlines in different wall-normal locations.

This chapter includes the results of PERVEN, R., PHILIP, J., KLEWICKI, J. 2019 Statistical properties of streamline geometry in turbulent wall-flows. Phys. Rev. Fluid. (In Production.)

4.1 Curvature

The curvature of a streamline measures the deviation of the streamline from being a straight line (bending). In a turbulent flow, the streamline pattern changes from one instant to the next. Thus, the curvature components in the streamwise κ_x, wall normal κ_y and spanwise, κ_z directions (equation 3.20) measured at any given fixed point in space are fluctuating quantities. For this reason, we investigate the statistical properties of κ and τ, e.g., the mean ($\overline{\kappa} = \sum \kappa_i/N$) and the standard deviation ($\sigma_\kappa = \sqrt{\sum (\kappa_i - \overline{\kappa})^2/N}$), where N is the size of the curvature ensemble. In what follows, u, v and w are the fluctuating streamwise x, wall-normal y,

and spanwise z velocity components and unless otherwise noted all quantities are normalized by kinematic viscosity ν and friction velocity u_τ. The total, mean and fluctuating streamwise velocity components are defined as $\tilde{u}, U$ and u respectively i.e., $\tilde{u} = U + u$, and similarly for the wall-normal and spanwise components. The curvatures computed from the total and fluctuating field are defined as $\tilde{\kappa}$ and κ respectively.

Large values of curvature are associated with the small length scale features of the turbulent flow and vice versa. As such it can be reasoned that curvature tends to attain extreme values near a stagnation point either in a fixed frame for a zero mean flow field or relative to a mean flow [Schaefer, 2012]. The radius of curvature has also been shown to be comparable to the Taylor microscale in the isotropic flow [Schaefer, 2012]. Thus, here we compare the inverse of the curvature magnitude (radius of curvature) with the Taylor microscale in the inertial layer. This connects to the study [Dallas *et al.*, 2009] (described in the literature review chapter) indicating that the distance between stagnation points is proportional to the Taylor microscale. The Taylor microscale scales with the square root of wall location in the inertial layer, as following.

Classical theoretical analysis of the turbulence energy equation in wall-flows indicates that the energy production $\wp$ is approximately equal to the dissipation rate in the inertial (logarithmic) layer Tennekes & Lumley [1972]. Accordingly, the dissipation rate, $\epsilon \approx \wp = \langle\overline{uv}\rangle \partial U/\partial y$. On the other hand, dissipation can be reasonably obtained from the isotropic estimate, $\epsilon_{iso} = 15\nu\sigma_u^2/\lambda^2$, where λ is the Taylor microscale and σ_u is the standard deviation of u for the fluctuating flow field. Assuming the usual log law for $U(y)$ (i.e., $U^+ = 1/k \ln(y^+) + \text{const.}$), $\wp = \langle\overline{uv}\rangle \partial U/\partial y \approx u_\tau^3/ky = \epsilon = 15\nu\sigma_u^2/\lambda^2$, where k is the von Kármán constant. From this (and noting that $\sigma_u \sim u_\tau$), it is apparent that λ^+ scales according to $\sqrt{y^+}$ in the inertial or the logarithmic layer of wall-flows.

Herein, the Taylor microscale, λ, is evaluated in two ways: based on the isotropic approximation and using the actual viscous dissipation rate. The actual viscous dissipation rate is $\epsilon = 2\nu\overline{s_{ij}s_{ij}}$, with $s_{ij} = (1/2)(\partial u_i/\partial x_j + \partial u_j/\partial x_i)$. Then using the relation for the dissipation in isotropic turbulence, $\epsilon_{iso} = 15\nu\overline{(\partial u_1/\partial x_1)^2} = 15\nu\sigma_u^2/\lambda^2$ e.g. Tennekes & Lumley [1972]. Thus, the Taylor microscale for isotropic turbulence can be defined as,

$$\lambda = \frac{\sigma_u}{\sqrt{\overline{(\partial u_1/\partial x_1)^2}}}, \tag{4.1}$$

and the Taylor microscale using the actual viscous dissipation rate is,

$$\lambda_\epsilon = \sqrt{\frac{15\nu}{\epsilon}}\sigma_u. \tag{4.2}$$

Before presenting the statistics of curvature, it is important to recognize that the mean of the curvature magnitude and component curvatures are not derivable from the mean streamlines. Rather, they derive from the instantaneous velocity field.

For example, the mean wall-normal velocity V for the channel flow is identically zero, but the mean of the curvature component associated with the wall-normal direction is non-zero, as described and discussed later. This is because the mean wall-normal curvature is computed from the instantaneous field, and is non-linearly related to the mean field.

Figure 4.1 presents the mean curvature statistics for the boundary layer and channel flows investigated. The grey dash lines in figure 4.1 indicate the position of the momentum balance layer boundaries associated with $\delta^+ = 1660$ (Table 1). This plot clarifies the variation of the mean statistics of curvature magnitude and curvature components with the wall-normal distance. Figure 4.1(a) shows the profiles of the mean curvature magnitude $\overline{\tilde{\kappa}^+}$ versus y^+. For comparison, we also plot the inverse of the inner normalized Taylor microscales given by equations. 4.1 (denoted by the dot symbols) and 4.2 (denoted by the cross symbols). Here, $\overline{\tilde{\kappa}^+}$ decreases with the wall-normal distance, except in a region between $y^+ \simeq 15$ to $y^+ \simeq 50$ in layer II (see figure 4.1(c)). From there $\overline{\tilde{\kappa}^+}$ exhibits an approximate power-law decrease and continues this decrease into the inertial layer (layer IV). The power law slope is about -0.5, which is the value expected if $\tilde{\kappa}$ scales like the estimate for $1/\lambda$ indicated above. Overall, these results indicate that the streamlines with large mean curvature values are located close to the wall.

We now compare the mean curvature magnitude with the Taylor microscales denoted by the dot and the cross symbols in the upper curve of figure 4.1(a). It is difficult to measure the derivatives in s_{ij} tensor (above) through experiments wherein mostly the streamwise velocity component is measured. Hence, for practical reasons, the isotropic estimate is typically employed. This isotropic approximation works well away from the near-wall region [Klewicki & Falco, 1990] and this is also evidenced in figure 4.1(a). Here, the difference between the profiles of $1/\lambda^+$ and $1/\lambda_\epsilon^+$ near the wall is clearly evident. These profiles then coincide beginning near the outer portion of layer II. The experimental data by Vincenti *et al.* [2013] denoted by the pink square symbol also merge with these $1/\lambda^+$ and $1/\lambda_\epsilon^+$ profiles (using the current DNS data) from the same position in layer II and into the outer region.

The grey dotted line of figure 4.1 (a) at $y^+ = 262$, displays the upper bound for the classical log layer of $y/\delta = 0.2$ in case of $\delta^+ = 1660$. The mean curvature magnitude at this location is not proportional to $1/\lambda^+$ as it decays with a somewhat different slope of about -0.3. This is close to, but deviates from the estimates of equation 4.1 or equation 4.2. Thus, in the inertial region, the radius of curvature $(1/\overline{\tilde{\kappa}})$ has a power law that varies similarly to λ but with a somewhat different magnitude. A similar result is also evidenced in figure 4.9 below.

We now investigate the wall-normal profiles of the mean curvature components in the streamwise, wall-normal and spanwise directions as defined by equation 3.20. Figure 4.1(b)) displays the mean streamwise curvature ($\overline{\tilde{\kappa}_x^+}$) with y^+. Similar to $\overline{\tilde{\kappa}^+}$, $\overline{\tilde{\kappa}_x^+}$ shows a decreasing behaviour with increasing distance from the wall and an approximate power law decrease across layer IV. In the region between $y^+ \simeq 15$ to $y^+ \simeq 50$, however, the $\overline{\tilde{\kappa}_x^+}$ profile is nearly constant as shown in figure 4.1(d).

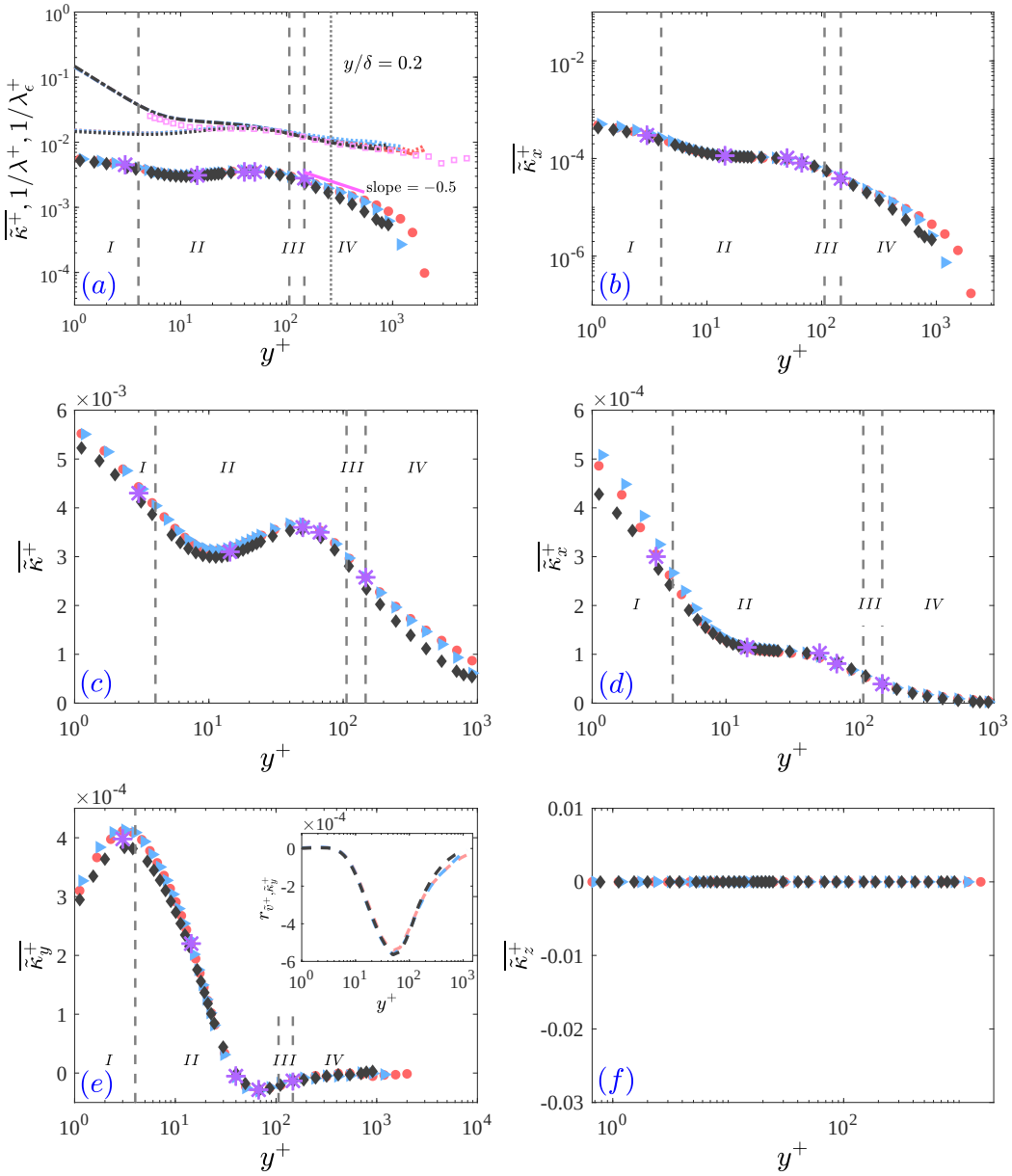

FIGURE 4.1: Mean statistics of curvature in case of the boundary layer (circle symbols used for $\delta^+ \approx 2530$ and arrow symbols are for $\delta^+ \approx 1660$) and the channel flow (diamond symbols are used for $\delta^+ \approx 934$). Dashed lines represent the layer boundaries associated with the mean momentum equation (Table 1) corresponding to $\delta^+ = 1660$. Stars are some positions where the pdfs have been calculated that shown in figure 4.7. **(a)** Mean of curvature magnitude with the inverse of Taylor microscale (dotted symbol using equation 4.1 and dashdot symbol using equation 4.2). Square symbol is the experimental data from [Vincenti *et al.*, 2013] for $\delta^+ \approx 6430$. **(b)** Mean streamwise curvature **(c)** The mean of curvature magnitude in log-linear scale **(d)** The mean streamwise curvature in log-linear scale **(e)** Mean wall-normal curvature, The inset represents the correlation of the wall-normal curvature with the wall-normal velocity. **(f)** Mean spanwise curvature

With increasing distance from the wall, it is probably safe to surmise that the instantaneous streamlines become increasingly aligned in the x-direction, and thus the largest $\overline{\tilde{\kappa}_x^+}$ values are observed close to the wall.

Figures 4.1(c) and 4.1(d) respectively show $\overline{\tilde{\kappa}^+}$ and $\overline{\tilde{\kappa}_x^+}$ on a log-linear scale. These figures allow a deeper investigation of the profile structure across layer II. The mean curvature magnitude in figure 4.1(c) shows a clear increasing behaviour between $y^+ \simeq 15$ to $y^+ \simeq 50$ in layer II, i.e. from the peak in the turbulence kinetic energy to close to the region where advection dominates vorticity transport [Klewicki, 2013*a*] (see Introduction: section A). The intermediate rise of $\overline{\tilde{\kappa}^+}$ in the region $15 \lesssim y^+ \lesssim 50$ is consistent with the lifting and roll-up of near-wall shear layer-like motions e.g., Johansson *et al.* [1991], Klewicki & Hirschi [2004]. In this region, vorticity stretching is large and this mechanism leads to a reduction in the scale of the high vorticity motions. This provides a rational explanation for the increase in $\overline{\tilde{\kappa}^+}$. Beyond $y^+ \simeq 50$, vorticity advection leads to a spatial dispersion of vorticity that, as a mechanism, increasingly dominates with increasing y^+ [Klewicki, 2013*a*]. Consistent with this, the curvature values start decreasing for $y^+ > 50$.

The behaviour of the mean curvature components in the x, y and z directions in figures 4.1(d), (e) and (f) are different from the mean curvature magnitude $\overline{\tilde{\kappa}^+}$ in figure 4.1(c). In particular, $\overline{\tilde{\kappa}_x^+}$ in figure 4.1(d) shows a constant plateau in the region of the intermediate increase in figure 4.1(c). On the other hand, $\overline{\tilde{\kappa}_y^+}$ (figure 4.1(e)) shows decreasing behavior across that region, while $\overline{\tilde{\kappa}_z^+}$ (figure 4.1(f)) is zero everywhere. The $\overline{\tilde{\kappa}_y^+}$ result is considered later to investigate the origin of its non-zero values in the region close to the wall. These component-wise comparisons indicate that figure 4.1(c) cannot be determined as a composite of figures 4.1(d), (e) and (f).

Figure 4.1(e) presents the mean wall-normal curvature ($\overline{\tilde{\kappa}_y^+}$) with y^+. The profiles exhibit a positive peak near the outer edge of layer I and a slightly negative peak near the outer edge of layer II, with a rapid decay in between. In layer IV, the $\overline{\tilde{\kappa}_y^+}$ profiles remain almost constant with a value nearly equal to zero. Here, for a channel flow, in spite of $\tilde{V} = 0$, $\overline{\tilde{\kappa}_y^+} \neq 0$. This is because the mean wall-normal curvature component for the instantaneous flow field is not directly determined by the corresponding wall-normal velocity component. Rather, it is an indication of the curvature of the ensemble of streamlines. This means κ_y does not only depend on the fluctuating wall-normal velocity, but also on the other fluctuating velocity components. These effects are further clarified in the pdf results in the next section, while below we examine the relationship between the v and κ_y fluctuations.

To clarify the relationship between the wall-normal velocity component with the wall normal curvature component, the inset plot of figure 4.1(e) presents the correlation between $\tilde{\kappa}_y^+$ and $\tilde{v}^+$ versus y^+. The correlation function is computed using,

$$r_{\tilde{v},\tilde{\kappa}_y} = \frac{1}{N}\sum_{i=1}^{i=N} v\kappa_y = \overline{v\,\tilde{\kappa}_y} \tag{4.3}$$

and the correlation coefficient is given by,

$$R_{\tilde{v},\tilde{\kappa}_y} = \frac{1}{N}\frac{\sum_{i=1}^{i=N} v\kappa_y}{\sigma_{\tilde{v}}\sigma_{\tilde{\kappa}}} = \frac{\overline{v\,\tilde{\kappa}_y}}{\sigma_{\tilde{v}}\sigma_{\tilde{\kappa}}}, \tag{4.4}$$

where N is the size of the ensemble. The correlation is slightly positive close to the wall and then negative elsewhere, with a negative peak at $y^+ \approx 50$. Thus, except very near the wall, the wall-normal velocity $\tilde{v}^+$ and the associated curvature $\tilde{\kappa}_y^+$ are anti-correlated. Physically, this means that the combinations of positive and negative $\tilde{v}$ and $\tilde{\kappa}_y$ add up to a larger value, so that the wall-normal curvature is negative for the positive wall-normal velocity (flow away from the wall) and positive for the negative wall-normal velocity (wall-ward flow). This means, relative to a quadrant decomposition involving $\tilde{v}$ and $\tilde{\kappa}_y$, the second and fourth quadrants are most heavily weighted.

The mean spanwise curvature ($\overline{\tilde{\kappa}_z^+}$) values in figure 4.1(f) are essentially zero for all y^+ locations. Note that, these zero values of $\overline{\tilde{\kappa}_z^+}$ are not a consequence of the spanwise homogeneity, as then $\overline{\tilde{\kappa}_x^+}$ in figure 4.1(b) would also be zero for fully developed flow. Here, this zero results come from the negligible values of the spanwise tangent vector derivative between two consecutive points of the flow field. Qualitatively, the mean statistics of curvature magnitude and curvature components show similar behaviour for the boundary layers and the channel DNS employed.

4.1.1 Behaviour of the wall-normal curvature near the wall

An interesting result of the mean statistics in figure 4.1(e), is the positive peak of $\overline{\tilde{\kappa}_y^+}$ near the outer edge of layer I. The origin and nature of this near-wall positive wall-normal curvature peak are explored further in figures. 4.2-4.5.

Figure 4.2(a) presents a streamline pattern with the concave upward and concave downward peak denoted by the arrows. The upward (A) and downward (B) double arrows show the inflection segments where sign changes happen between the concave up to concave down streamline shape. Note that the sign of the wall-normal curvature κ_y is determined by the direction of a vector from the curve to its center of curvature. Here, $\tilde{\kappa}_y$ is positive in the concave upward segment and negative in the concave downward segment, as denoted by the arrows on the streamline in figure 4.2(a). This means that the concave upward peak position on a streamline, e.g., center of curvature points away of wall, corresponds to a positive peak value of $\tilde{\kappa}_y$ and the concave downward peak on the streamline, i.e. center of curvature pointing towards the wall, corresponds to a negative peak value of $\tilde{\kappa}_y$. As shown in figure 4.2(a), the arrows show the center of curvature which is related to the inverse of curvature (radius) at the arrow starting point. From this, one therefore expects that at the positive peak in figure 4.1(e), streamlines of the orientation associated with the upward arrow of figure 4.2(a) are prevalent.

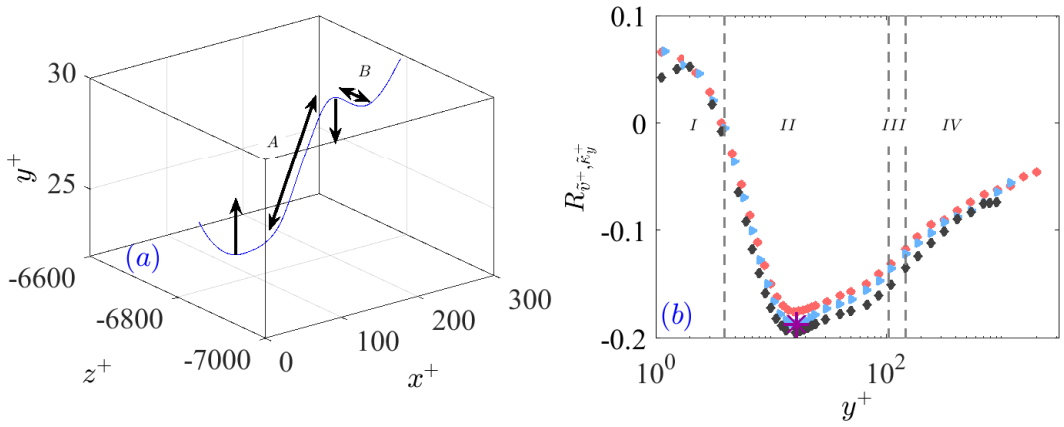

FIGURE 4.2: **(a)** Configuration that depicts positive κ_y near $y^+ = 24$. The up and down arrows denote the local radius of curvature and the sign of κ_y relative to the indicated minimum wall-normal location of the streamline. The inclined double arrows at "A" and "B" indicate the inflection part on this streamline. **(b)** The correlation coefficient of $\tilde{v}^+$ and $\tilde{\kappa_y}^+$ in case of the boundary layer (circle symbols are used for $\delta^+ \approx 2530$ and arrow symbols are for $\delta^+ \approx 1660$) and the channel flow (diamond symbols are used for $\delta^+ \approx 934$). The dashed lines represent the layer boundaries associated with the mean momentum equation (Table 1) corresponding to $\delta^+ = 1660$. At the star position, the conditional averages have been computed in figures. 4.3(b), 4.3(d) and 4.4(b)

To clarify the directional sign changes of κ_y along the streamline pattern of figure 4.2(a), all four possible cases are shown by the arrows and double arrows. The four cases arise from the positive and negative sign combinations of $\tilde{\kappa_y}$ and $\tilde{v}$. The region on the streamline adjacent to the upward arrow is a case where $\tilde{\kappa}_y$ is positive but $\tilde{v}$ changes sign from negative to positive before and after the position of the arrow. Similarly, near the downward arrow, $\tilde{\kappa}_y$ is negative but $\tilde{v}$ changes sign from positive to negative before and after the arrow position. For the first inflection region denoted by A in figure 4.2(a), $\tilde{v}$ is positive but $\tilde{\kappa_y}$ changes sign from positive to negative. Similarly, for the second inflection region denoted by B, $\tilde{v}$ is negative but κ_y changes sign from negative to positive. Collectively, these cases just described, characterize the conditions for which the sign of the $\tilde{v}$ and $\tilde{\kappa_y}$ product is determined.

Figure 4.2(b) shows the correlation coefficient of $\tilde{v}^+$ and $\tilde{\kappa}_y^+$ denoted by $R_{\tilde{v}^+,\tilde{\kappa}_y^+}$ for the considered boundary layer and channel DNS. This plot reveals negative values except in layer I, where $\tilde{v}^+$ and $\tilde{\kappa}_y^+$ exhibit a weakly positive correlation. This plot also reveals an anti-correlation peak of $R_{\tilde{v}^+,\tilde{\kappa}_y^+}$ at $y^+ \approx 17$, i.e. near the peak in the turbulence kinetic energy. The correlation function $r_{\tilde{v}^+,\tilde{\kappa}_y^+}$ shown in the inset plot of figure 4.1(e) shows only a mild negative value at this peak negative position for $R_{\tilde{v}^+,\tilde{\kappa}_y^+}$. On the other hand, $r_{\tilde{v}^+,\tilde{\kappa}_y^+}$ shows a peak negative value at $y^+ \approx 50$. Thus, the shape of $R_{\tilde{v}^+,\tilde{\kappa}_y^+}$, and $r_{\tilde{v}^+,\tilde{\kappa}_y^+}$ are distinctly different. Since $\sigma_{\tilde{\kappa}_y^+}$ is approximately constant (as discussed later relative to figure 4.6(c)), this shape difference of $R_{\tilde{v}^+,\tilde{\kappa}_y^+}$, and $r_{\tilde{v}^+,\tilde{\kappa}_y^+}$ comes from the significant variation in the

fluctuating wall-normal velocity variance with y^+. At this peak negative $R_{\tilde{v}^+,\tilde{\kappa}_y^+}$ location the conditional averages have been computed and are compared below.

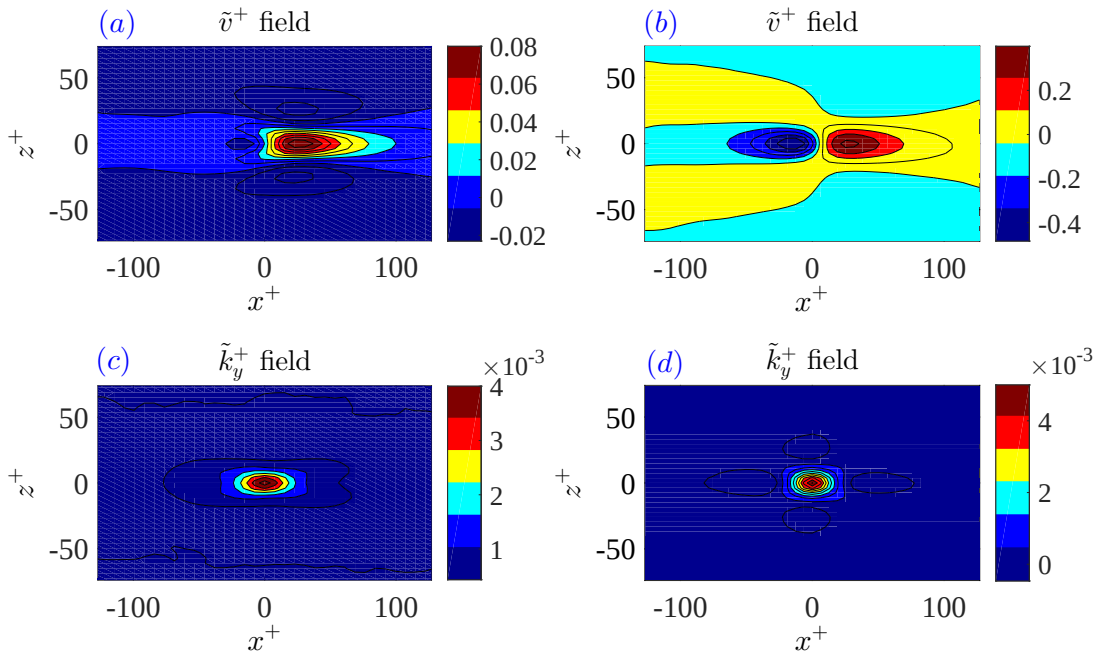

FIGURE 4.3: **(a)** Conditional average of $\tilde{\mathbf{v}}$ corresponding to positive $\tilde{\kappa}_y$ at $y^+ \approx 3$ for channel flow at $\delta^+ = 934$ **(b)** Conditional average of $\tilde{v}^+$ corresponding to positive $\tilde{\kappa}_y^+$ at $y^+ \approx 17$ for boundary layer flow at $\delta^+ = 2530$ **(c)** Average positive $\tilde{\kappa}_y^+$ at $y^+ \approx 3$ for channel flow at $\delta^+ = 934$ **(d)** Average positive $\tilde{\kappa}_y^+$ at $y^+ \approx 17$ for boundary layer flow at $\delta^+ = 2530$

The noted anti-correlation of the wall-normal velocity and the wall-normal curvature is also examined by the conditional average of $\tilde{v}^+$ corresponding to $\tilde{\kappa}_y^+$ in figures 4.3-4.5. Figure 4.3(a) is the average of $\tilde{v}^+$ conditioned on positive $\tilde{\kappa}_y^+$ values in the xz-plane at $y^+ \approx 3$ for channel flow, i.e., at the positive peak of figure 4.1(e). Figure 4.3(b) is the average $\tilde{v}^+$ conditioned on positive $\tilde{\kappa}_y^+$ at the negative peak of $R_{\tilde{v}^+,\tilde{\kappa}_y^+}$ at $y^+ \approx 17$ for the boundary layer flow. Recall that, the statistical results for the boundary layer and channel flow show similar behaviour. The averages of the positive $\tilde{\kappa}_y^+$ values are shown in figures. 4.3(c) and 4.3(d) at $y^+ \approx 3$ (channel flow) and at $y^+ \approx 17$ (boundary layer flow) respectively. Note that the colorbar scaling is not the same for all figures owing to the small ranges associated with the color contours. To better understand the location of the positive peak of $\tilde{\kappa}_y^+$ (deep red region in Figs. 4.3(c) and 4.3(d)) relative to the $\tilde{v}^+$ field, figures. 4.3(c) and 4.3(d) are superimposed on figures. 4.3(a) and 4.3(b), respectively and shown in figures. 4.4(a) and 4.4(b). The positive peak region of $\tilde{\kappa}_y^+$ is shown by the pink line contour. The anti-correlation property of $\tilde{v}^+$ and $\tilde{\kappa}_y^+$ nominally coincides with the condition where the pink contour of $\tilde{\kappa}_y^+$ overlaps with the peak negative region of $\tilde{v}^+$.

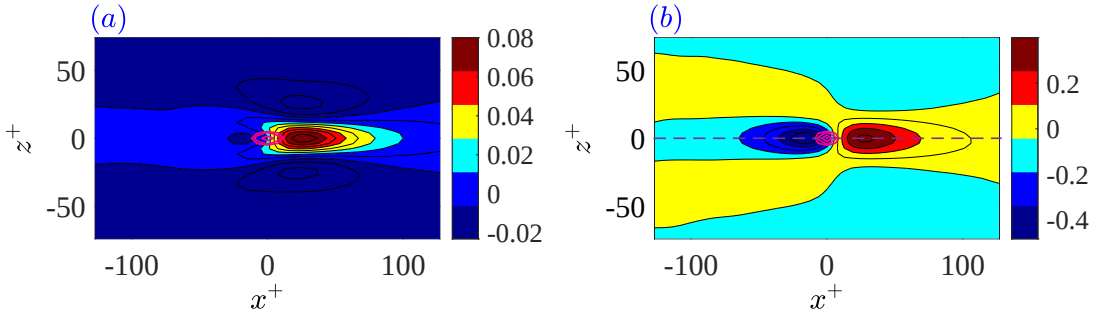

FIGURE 4.4: **(a)** Peak positive contour of $\tilde{\kappa}_y^+$ (figure 4.3(c)) superimposed on the corresponding conditional $\tilde{v}^+$ contour (figure 4.3(a)). **(b)** Peak positive contour of $\tilde{\kappa}_y^+$ (figure 4.3(d)) superimposed on the corresponding conditional $\tilde{v}^+$ contour (figure 4.3(b))

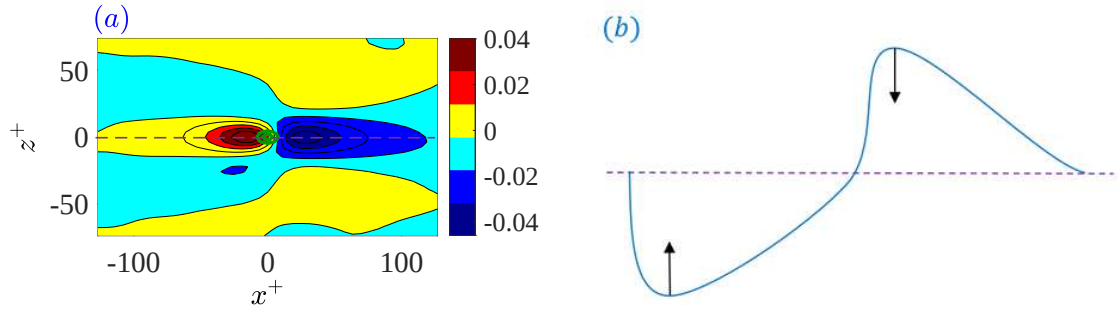

FIGURE 4.5: (a) Conditional average of $\tilde{v}^+$ corresponding to negative $\tilde{\kappa}_y^+$ grids at wall-normal position $y^+ \approx 3$ in case of boundary layer flow case at $\delta^+ = 2530$ (b) Sketch of the corresponding streamline for varying x^+ along $z^+ = 0$ as denoted by purple dash line in (a) and in figure 4.4 (b)

Close to the wall, $y^+ \approx 3$ (figure 4.4(a)), the positive wall normal curvature contours are nearly equally distributed between the positive and negative contours of v. This is because of the nearly symmetric probability of positive and negative v fluctuations for positive κ_y. To better understand this structure we draw reference to the upward arrow in figure 4.2(a) where the positive κ_y values correspond both the positive and negative v values. At $y^+ \approx 17$ (figure 4.4(b)), positive $\tilde{\kappa}_y^+$ contours now reside more prevalently in the negative peak region of $\tilde{v}^+$. Thus, this case implies that for a situation like that near the upward arrow of figure 4.2(a), the positive κ_y values mostly correspond to a steep wall-ward trajectory, followed by a shallow trajectory away from the wall. This is also consistent with the correlation coefficient results in figure 4.2(b) where $\tilde{\kappa}_y^+$ and $\tilde{v}^+$ are anti correlated except very near the wall.

To reinforce this anti-correlation result of figure 4.4(b)), figure 4.5 (a) shows the complementary conditional average. That is, the average of $\tilde{v}^+$ conditioned on negative $\tilde{\kappa}_y^+$ values at $y^+ \approx 17$ for the boundary layer flow case. As expected, the green contours presenting negative peak region of $\tilde{\kappa}_y^+$, reside more prevalently in the positive $\tilde{v}^+$ region. Here, this case implies that for a situation like near

the downward arrow of figure 4.2(a) the negative κ_y values mostly correspond to a steep trajectory away from the wall, followed by a shallow wall-ward trajectory. Figure 4.5 (b) shows a streamline pattern consistent with the dashed centre line of figures. 4.4 (b) and 4.5 (a) by the streamline portions below and above the dashed line, respectively. Thus, figure 4.5 (b) contains representative features associated with a streamline pattern consistent with figures. 4.4 (b) and 4.5 (a). Here, the anti-correlation case of figure 4.4 (b) (positive $\tilde{\kappa}_y^+$ and negative $\tilde{v}^+$) corresponds to the streamline pattern below the dashed line of figure 4.5 (b), while, the anti-correlation case of figure 4.5 (a) (negative $\tilde{\kappa}_y^+$ and positive $\tilde{v}^+$) corresponds to the streamline pattern above the dashed line. Thus, the peak positive value of $\overline{\tilde{\kappa}_y^+}$ in figure 4.1(e) corresponds to the concave upward peak region on a streamline pattern like that of the streamline pattern below the dashed line in figure 4.5 (b)) with the steep wallward v and with the centre of curvature pointing away from the wall. Here, the concave upward shape of this streamline (associated with positive κ_y) occurs in concert with a strong wallward v followed by a weaker v flow away from the wall. Therefore, the positive peak of $\overline{\tilde{\kappa}_y^+}$ in figure 4.1(e) is associated with strong wallward v velocities as depicted.

4.1.2 Standard deviation relative to mean curvature

The ratio of the mean curvature to the standard deviation provides an indication of the relative importance of the fluctuations. Figure 4.6 presents the ratio of the mean curvature to standard deviation versus y^+. The dash lines are again the momentum balance layer boundaries for $\delta^+ \approx 1660$ according to Table 1. Figure 4.6(a) shows the profiles of the ratio of the mean to standard deviation for the curvature magnitude. This ratio has its lowest value near the wall, and increases with distance from the wall. The ratio reaches a peak value near the onset of the inertial region, i.e., near the outer edge of layer III. After that, it attains a plateau near unity, dropping off slowly in the log layer, and then more drastically in the outer region. Thus, the curvature variance is larger than the mean out to a position near the outer edge of layer II. From layer III, the variance becomes slightly smaller than the mean until the center of layer IV, after which it becomes larger than the mean out to $y^+ \simeq \delta$. Thus, this plot reveals that the lowest curvature fluctuation relative to the mean occurs near the onset of the inertial layer.

Figure 4.6(b) shows the ratio of the mean to the standard deviation for the streamwise curvature component. In this case, the ratio shows an increasing trend up to a peak near the outer edge of layer II and then decreases across the log layer. This indicates that the minimum average fluctuation relative to the mean occurs near the outer edge of layer II. The ratio for the wall-normal curvature, figure 4.6(c) behaves in the similar trend as $\overline{\tilde{\kappa}_y^+}$ in figure 4.1(e). This plot also shows a positive peak at the same wall location as the positive peak of figure 4.1(e). After the peak value, it decreases rapidly and remains constant from the outer edge of layer II outward. This figure reveals that the variance of κ_y remains approximately constant across the flow.

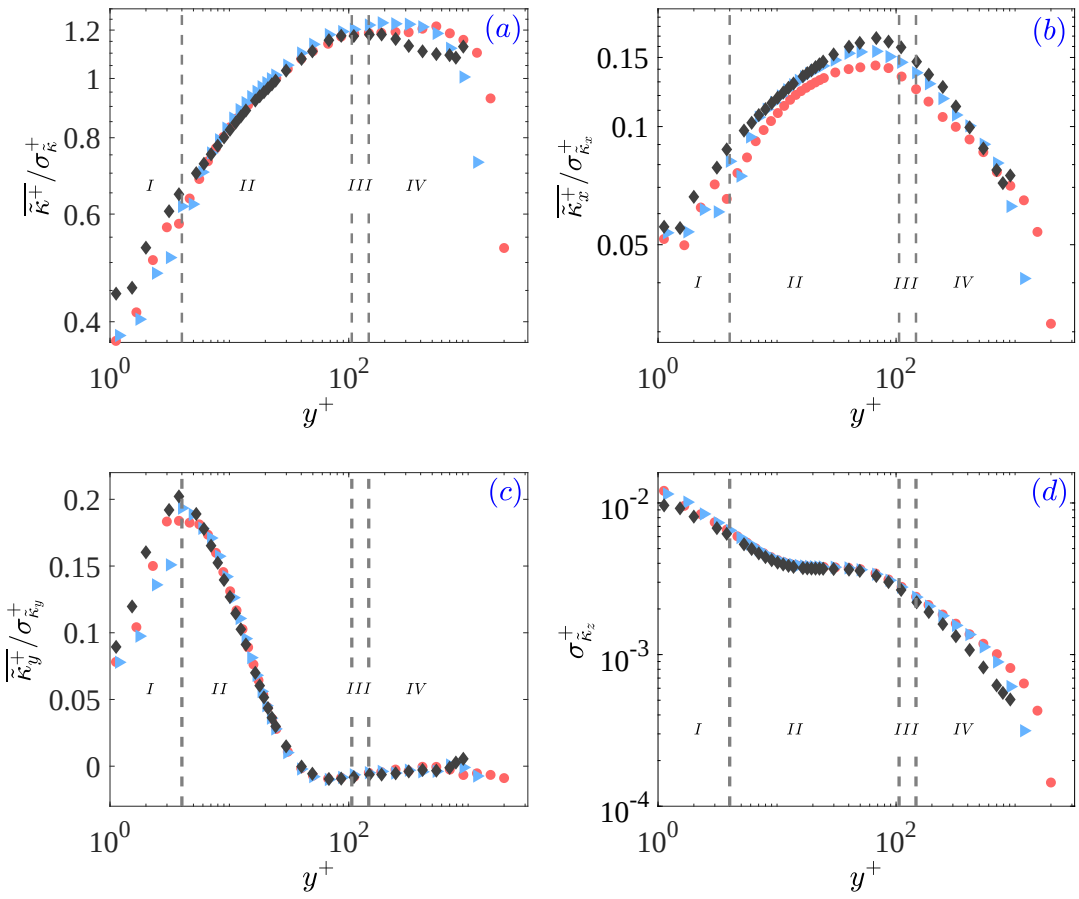

FIGURE 4.6: The ratio of the mean and standard deviation of the curvatures in case of the boundary layer (circle symbols are used for $\delta^+ \approx 2530$ and arrow symbols are for $\delta^+ \approx 1660$) and the channel flow (diamond symbols are used for $\delta^+ \approx 934$). The dashed lines represent the layer boundaries associated with the mean momentum equation (Table 1) corresponding to $\delta^+ = 1660$. **(a)** Curvature magnitude ratio **(b)** Streamwise curvature ratio **(c)** Wall-normal curvature ratio and **(d)** Standard deviation of curvature in the spanwise direction

Figure 4.6(d) presents the standard deviation of $\tilde{\kappa}_z^+$. Note that, the ratio for the spanwise case has negligible value as $\overline{\tilde{\kappa}_z^+} \cong 0$ everywhere (figure 4.1 f). This figure shows a decreasing magnitude with distance from the wall similar to $\overline{\tilde{\kappa}^+}$ in figure 4.1(a). All the ratios in figure 4.6 show that the maximum variances relative to the mean occur near $y^+ \simeq 0$, and near $y^+ \simeq \delta$.

The mean and standard deviation of curvature profiles in figure 4.1 and figure 4.6 are derived from the total velocity field exhibit both decreasing and increasing trends with wall-normal position. These statistics indicate that the streamlines with large curvature values are generally concentrated closer to the wall. The actual distribution of curvatures can, however, be analyzed in greater depth by the probability density functions at locations of interest. The next section covers the properties of curvature pdfs as derived from both the total and fluctuating velocity fields at the positions denoted by the stars in figure 4.1.

4.2 Probability density function of curvatures

The distribution of curvature values at a given wall-normal location contains information about the scales of motion at that location. For isotropic flow, Schaefer [2012] found that for a range of large curvatures (small scale motions), the pdf of κ exhibited exponential tails with a power-law slope of -4, which can be derived under reasonable assumptions as mentioned in the introduction of this paper. Physically, large values of curvature are associated with small length scales of the turbulent flow and vice versa. When these small length scales become smaller than the Kolmogorov length scale η, they cannot correspond to any geometrical features of the energetic turbulence. Conceptually, the exponent of -4 is the scaling associated with for these extreme curvature values. When rescaled by the -4 factor, these motions become comparable to those associated with length scales $\geq \eta$. Streamlines approaching a stagnation point are sharply deflected. Thus, as Schaefer describes, it is expected that the stagnation point structure causes these extreme values of curvature. This finding is reinforced in the present joint pdf results section.

Figure 4.7 presents the pdf of curvatures at wall-normal locations of interest. These positions are denoted by stars in figure 4.1. Here, the pdfs results are computed using the $\delta^+ = 2530$ boundary layer DNS. The left side plots of figure 4.7 are computed using the total velocity field, while the right side results are calculated using the fluctuating velocity field. The solid blue line represents a power function with an exponent of -4.

Figure 4.7(a) shows the pdfs of curvature magnitude ($\tilde{\kappa}^+$) where different symbols are for the pdf at different y^+. Here, the exponent of -4 is only apparent close to the wall. For fluctuating velocity fields in figure 4.7(b), however, -4 scaling is more apparent away from the wall.

Figures 4.7(c) and 4.7(d) show the streamwise curvature pdfs. Here, $P(\tilde{\kappa}_x^+)$ for both total and fluctuating velocity fields are qualitatively similar with different magnitudes and exhibit -4 scaling for positions away from the wall. Distinct from this, the wall-normal curvature pdfs in figures. 4.7(e) and 4.7(f) for the total and fluctuating streamlines are different. For the total velocity field, the $P(\tilde{\kappa}_y^+)$ profiles fall on top of each other for different wall-normal locations, and they do not follow -4 scaling except possibly for a small region near the wall. On the other hand, in figure 4.7(f) $P(\kappa_y^+)$ varies with wall-positions and follows -4 scaling at positions away from the wall. Here it is important to recognize that, if κ_y were to depend only on v, then the calculations using the total and fluctuating cases would be the same, since the mean V is zero (for channel flow). This is not the case, however, as κ_y does not depend on only v but also on the other velocity components. To further investigate the different behavior of the pdfs for total and fluctuating flow fields, the velocity field contours, and their corresponding streamlines are presented and described later relative to figure 4.12.

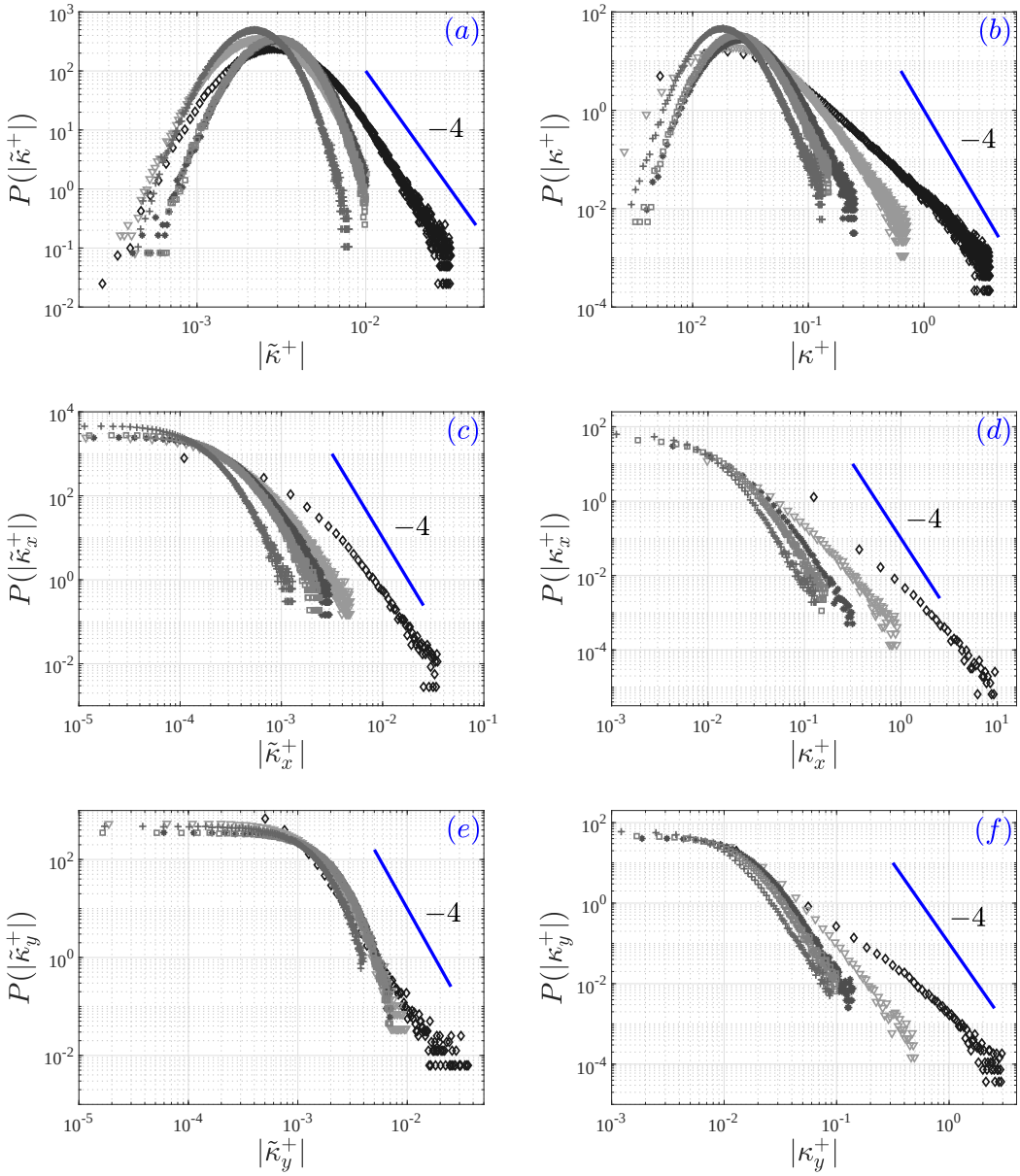

FIGURE 4.7: Probability density function of the curvature magnitude and curvature components at varying wall-normal locations; diamond, $y^+ = 3$; up arrow, $y^+ = 14$, star, $y^+ = 40$, square, $y^+ = 67$; plus, $y^+ = 174$. (a) Probability of the curvature magnitude computed from the instantaneous streamlines pattern, (b) Probability of the curvature magnitude for the fluctuating streamlines pattern, (c) Probability of the streamwise curvature for the instantaneous streamlines pattern, (d) Probability of the streamwise curvature for the fluctuating streamlines pattern, (e) Probability of the wall-normal curvature for the instantaneous streamlines pattern, (f) Probability of the wall-normal curvature for the fluctuating streamlines pattern

A number of results in figure 4.7 indicate that the first appearance of -4 scaling depends on y^+. To examine the onset of this behaviour, figure 4.8 presents the pdfs multiplied by the associated curvatures raised to the 4^{th} power at more

wall-positions than those considered in figure 4.7. The pink stars denote the approximate onset of -4 scaling. Figure 4.8(a) shows that κ^+ approximately follows the -4 scaling over a significant κ^+ range starting around $y^+ = 20$ outward for the fluctuating velocity field. The -4 scaling in figure 4.8(b) also starts near $y^+ = 20$. For the total velocity field in figure 4.8(c), however, the -4 scaling does not convincingly appear anywhere. Here, the most important observation is that with increasing y^+ a greater portion of the κ^+ and κ_y^+ pdfs adhere to -4 scaling. This correlates with the decreasing influence of viscous effects owing to a no-slip wall, with increasing y^+. Thus, the -4 scaling is apparently related to the fraction of the pdf associated with small scale motions. The onset of this scaling at different wall locations may correspond to features associated with the presence of stagnation points as described in the analysis of Schaefer [2012].

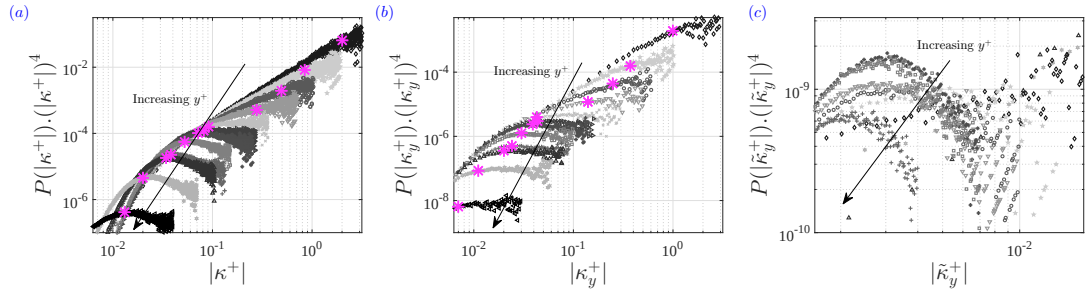

FIGURE 4.8: **(a)** -4 scaling for fluctuating velocity field ; **(b)** -4 scaling for velocity fluctuating field; **(c)** -4 scaling for total velocity field; at $y^+ = 3$, $y^+ = 7$, $y^+ = 10$, $y^+ = 14$, $y^+ = 21$, $y^+ = 31$, $y^+ = 40$, $y^+ = 67$, $y^+ = 147$, $y^+ = 192$, $y^+ = 703$, $y^+ = 1989$ starting from top. Pink stars denote the onset of -4 scaling.

Figure 4.9(a) provides insights that connect the onset of -4 scaling with the stagnation point studied by Vassilicos described in the literature. These studies demonstrate that the dissipation rate depends linearly on the density of the stagnation points in the logarithmic layer [Goto & Vassilicos, 2009]. This plot shows the onset of -4 scaling k_o (denoted by the pink stars in figure 4.8) with the inverse of the Kolmogorov scale. Here, η^+ has been computed based on both the isotropic approximation and the actual viscous dissipation rate. Namely, η^+ is calculated using $\epsilon = 15\nu\overline{(\partial u_1/\partial x_1)^2}$ and η_ϵ^+ is calculated using $\epsilon = 2\nu\overline{s_{ij}s_{ij}}$. Here, the profile characterizing the onset of -4 scaling has a significant deviation from the Kolmogorov scale near the wall up to near $y^+ \simeq 50$. For $y^+ \gtrsim 50$ these profiles then coalesce. On the inertial domain, both the onset of -4 scaling and the inverse of Kolmogorov scale varies as $1/y^+$.

Figure 4.9(b) shows the ratio of the Taylor microscale to the radius of curvature $(1/\overline{\kappa^+})$ at different wall-normal locations. Here, the two different symbols represent two different definitions of λ, where dot symbols use equation 4.1 and the cross symbols use equation 4.2. As discussed before, the isotropic formula is not a good approximation in the near-wall region. This is reflected by the deviation of the dot symbol up to $y^+ \simeq 50$. The cross symbol profiles (using the total dissipation

rate) indicate that the radius of curvature is greater than the intermediate scale λ^+ in layer I. From layer II, the radius of curvature becomes less than the Taylor microscale. This ratio shows a peak near the peak in the turbulent kinetic energy, i.e., near $y^+ \simeq 15$. After that, the ratio decreases gradually outward keeping the radius of curvature remain less than the Taylor microscale. Beyond $y^+ \simeq 50$, in layer III, the radius of curvature varies approximately in proportion to the Taylor microscale. In the inertial layer, this ratio varies approximately inverse with y^+.

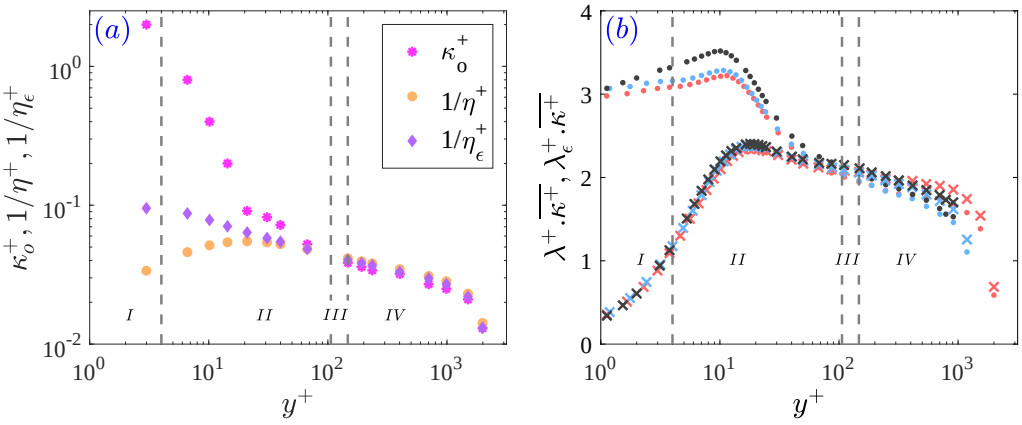

FIGURE 4.9: The grey dash lines indicate the position of the momentum balance layer boundaries associated with $\delta^+ = 1660$ (Table 1). **(a)** κ^+ (curvature magnitude for fluctuating streamlines) values at which -4 behaviour is first observed in the κ^+ pdf plot (figure 4.7(b)) versus y^+; i.e. the onset of -4 denoted by κ_o^+ has been presented as a function of y^+. Comparison is made between κ_o^+ and the inverse of Kolmogorov length scale $(1/\eta^+)$, where η^+ is computed from the total strain-rate and η_ϵ^+ is using the isotropic assumption; **(b)** Ratio of λ^+ (using the definitions from equations. 9 (dot symbols) and 10 (cross symbols)) and the inverse of curvature magnitude in case of the boundary layers (red symbols for $\delta^+ \approx 2530$; blue symbols for $\delta^+ \approx 1660$) and the channel flow (black symbols for $\delta^+ \approx 934$).

Figure 4.10 is the repetition of the previous results to clarify the statistics for the total and fluctuation curvature magnitude with Taylor microscale. These results show the curvature statistics using fluctuation velocity field scales as Taylor microscale better than that of using total velocity field.

Collectively, the above results draw interesting connections among the studies of Klewicki [2013*a*], Goto & Vassilicos [2009], Dallas *et al.* [2009], and Schaefer [2012]. As discussed in figure 4.1(c), Klewicki [2013*a*] showed that beyond $y^+ \simeq 50$ the mechanism of vorticity stretching significantly weakens and vorticity advection leads to the spatial dispersion of vorticity -a mechanism that increasingly dominates with increasing y^+. In the inertial domain, figure 4.9(a) shows that κ_o^+ varies proportionally to the inverse of the Kolmogorov scale, whereas the radius of curvature varies proportionally to the Taylor microscale as shown in figure 4.9(b); here, both results show inverse variation with y^+. These results follow those of Schaefer [2012] for isotropic flow. On the same domain, the density of stagnation points decreases like $1/y^+$ ([Dallas *et al.*, 2009]). This is consistent with the onset

of -4 scaling (figure 4.9(a)) that also decreases with y^+ within the same region. Here, $1/\kappa_o^+ \propto \eta^+$ and $1/\overline{\kappa^+} \propto \lambda$ beyond $y^+ \simeq 50$ and the non-proportionality before $y^+ \simeq 50$ arises from the overall effect of the presence of wall on the curvature. Rationally, these can stem from either viscous or wall-blocking effects. To better understand the wall-blocking limit, the pdf of wall-normal curvature is now analysed.

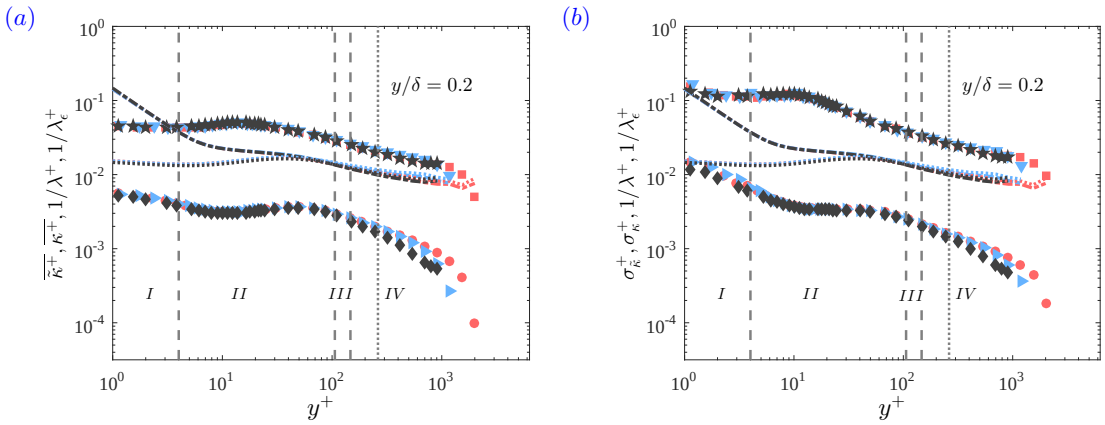

FIGURE 4.10: Mean statistics of curvature in case of the boundary layer (circle symbols used for $\delta^+ \approx 2530$ and arrow symbols are for $\delta^+ \approx 1660$) and the channel flow (diamond symbols are used for $\delta^+ \approx 934$). Dashed lines represent the layer boundaries associated with the mean momentum equation (Table 1) corresponding to $\delta^+ = 1660$. **(a)** Mean of curvature magnitudes using total and fluctuating velocity fields with the inverse of Taylor microscale (dotted symbol using equation 4.1 and dashdot symbol using equation 4.2). **(b)** Standard deviation of curvature magnitudes using total and fluctuating velocity fields with the inverse of Taylor microscale (dotted symbol using equation 4.1 and dashdot symbol using equation 4.2).

Figures 4.11(a), 4.11(b) and 4.11(c) present rectified pdfs for the positive and negative values of $\tilde{\kappa}_y^+$ at $y^+ = 3$, $y^+ = 10$ and $y^+ = 30$, respectively. For isotropic flow, the behaviour of the pdf tail is symmetric about its mean. Figures 4.11(a) and (b) reveal that the profiles for the positive and negative values of $\tilde{\kappa}_y^+$ are different near the wall. On the other hand, at $y^+ = 30$, Fig. 4.11(c) reveals that the positive and negative sides of $\tilde{\kappa}_y^+$ pdf are nearly symmetric. These results indicate a clear wall blocking effect (also shown later in Fig. 4.17) before $y^+ \approx 30$. Thus, the non-proportional results of Fig. 4.9 for $y^+ < 30$ are not for the viscous effect case. If so, then all the plots of Fig. 4.11 (within layer II where the viscous effect is on leading order) showed similar behaviour. Accordingly, approximately within $30 \leq y^+ \leq 50$, the non-proportional results of Figs. 4.9(a) and (b) occur for the viscous effect. Again from the plots of Fig. 4.11, it is predominant that the positive κ_y^+ profile follows -4 scaling nicely at $y^+ = 3$. Thus positive $\tilde{\kappa}_y^+$ values are mostly associated with the small scale motion of the flow at very close to the wall.

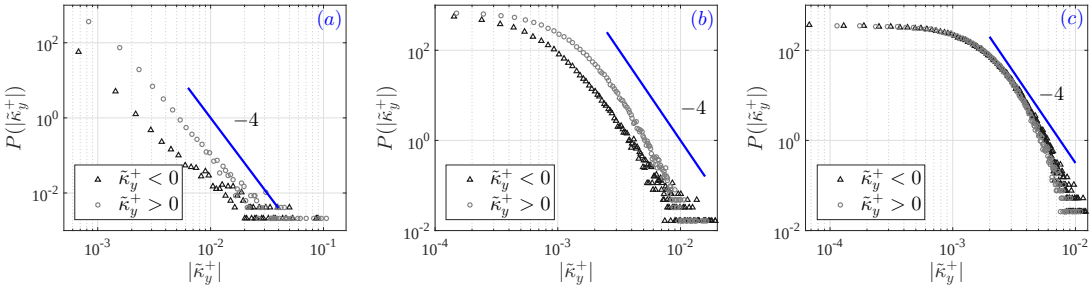

FIGURE 4.11: Pdf for positive and negative values of $\tilde{\kappa}_y^+$ at **(a)** the positive peak position of figure 4.1(e) i.e., at $y^+ = 3$; **(b)** at $y^+ = 10$; **(c)** at $y^+ = 30$

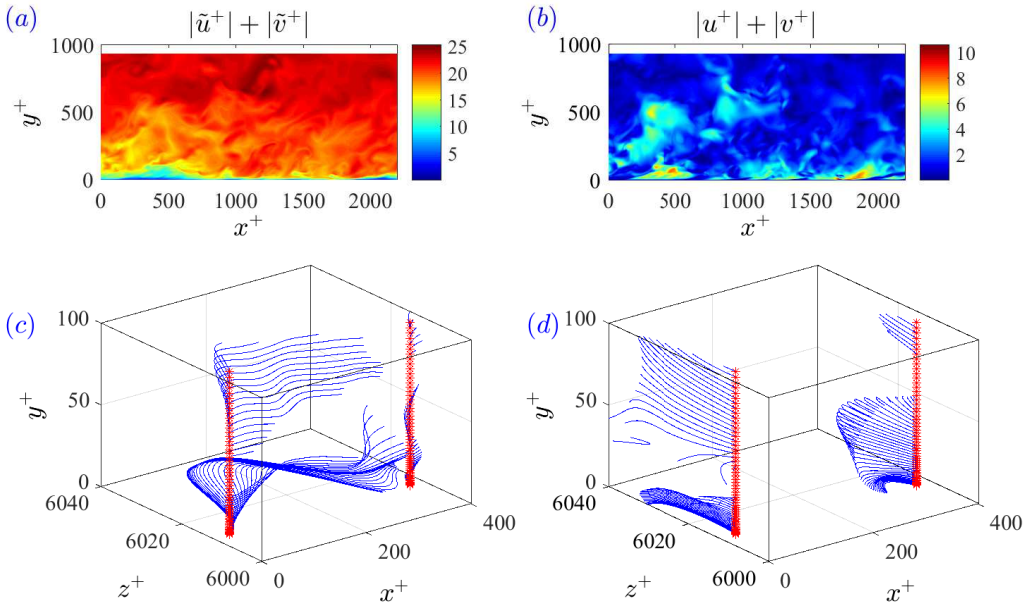

FIGURE 4.12: **(a)** Contour for total velocity field; **(b)** Contour for fluctuating velocity field; **(c)** Streamlines for the total velocity field; **(d)** Streamlines for the fluctuating velocity field

Figure 4.12 shows the velocity field contour (planar view) with the corresponding streamline pattern for the total (left side) and the fluctuating (right side) fields. From figures. 4.7, 4.8 and 4.10, we observe the different behaviour of curvature for the total, and fluctuating flow fields. Here, figure 4.12 shows the velocity fields and the streamlines pattern for the total and the subtracted mean flow fields physically. These plots clarifies the difference of streamlines pattern for the total velocity field and the mean subtracted velocity field. This change of the streamline pattern affects the total and component curvatures, that has observed already in the pdfs profiles of figure 4.7. Here, the positive and negative direction of the streamline twisting (figures. 4.12 (c) and (d)) i.e. torsion indicates the out of plane motion of the streamline. The statistical properties of the out of plane motion of the streamlines are analysed below.

4.3 Torsion

Torsion (τ) is a measure of the twisting of the streamlines out of a reference plane of motion. Similar to curvature, torsion is a length scale that defines the shape and size of the potential twisting of a streamline where the inverse of torsion means the radius of torsion. Torsion is positive or negative based on weather the streamline is moving with or counter to the binormal vector (section II(B)). Thus, positive and negative torsions are related to the out of plane motion rather than moving towards or moving away from the wall. For example, the torsion is positive for right-hand helix moving away from the wall but torsion is negative while also moving away from the wall for left-hand helix; and vice versa. In the present study, very small wall-normal length of the flow volume has been taken considering only two grid points before and two after at a particular wall-location to save CPU time and expense.

Figure 4.13(a) presents the mean torsion ($\overline{\tau^+}$) at different y^+ for the boundary layers and channel DNS employed. For the wall-normal length limitation of the flow volume, the twisting action is infinitesimal. For this reason, $\overline{\tau^+}$ values are very close to zero (slightly negative) in all y^+. If we consider the right-hand helix rule for the streamlines and employ the Frenet-Serret apparatus (section II(B)), the negative torsion reveals the streamlines are moving opposite to the binormal vector.

Figure 4.13(b) shows the standard deviation of torsion versus y^+. This plot has the maximum value at near-wall location and then it decreases with distance from the wall. This indicates that streamline patterns that twist out of the xz-plane are more prevalent in the near wall- region. Physically, this is consistent with the rapid three-dimensionalization of the velocity field near the wall.

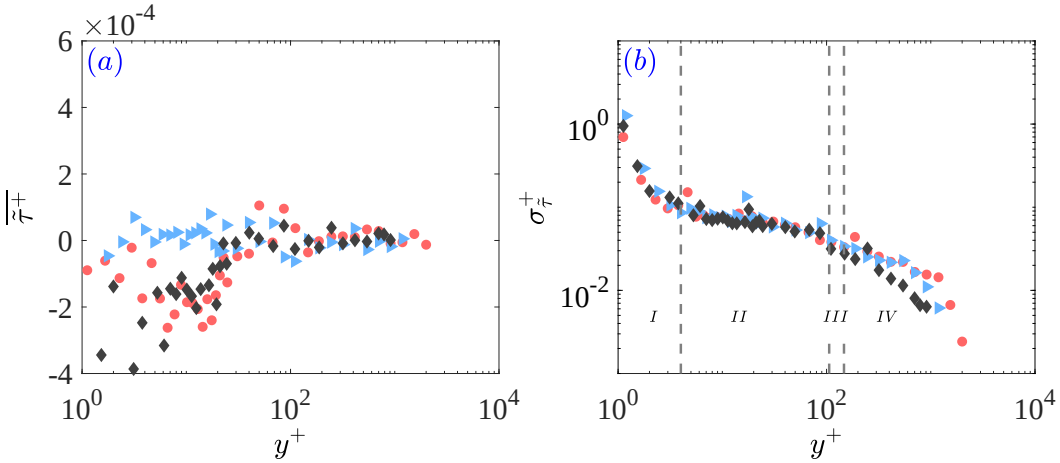

FIGURE 4.13: Torsion statistics of curvature in case of the boundary layer (circle symbols are used for $\delta^+ \approx 2530$ and arrow symbols are for $\delta^+ \approx 1660$) and the channel flow (diamond symbols are used for $\delta^+ \approx 934$). The dashed lines represent the layer boundaries associated with the mean momentum equation (Table 1) corresponding to $\delta^+ = 1660$. **(a)** Mean, **(b)** Standard deviation

We now compare the relative strength of bending and twisting of streamlines by examining the ratio of the curvature to the torsion across the flow. Figure 4.14(a) shows the ratio using the total velocity field at different wall-normal locations. The ratio has a maximum value close to the wall and then shows an approximately power law decay across layer II. Beyond $y^+ \simeq 50$ to the outer edge of the inertial layer, the ratio is constant with the positive values larger than 1. Figure 4.14(b) using the fluctuating velocity field also presents a similar decreasing behaviour up to the centre of layer II. The ratio starts to be constant at $y^+ \approx 17$, i.e., near the peak in the turbulent kinetic energy. Thus, this ratio reveals the more intense twisting motion than bending in all wall positions. Torsion required a reference plane to analyse the out of plane motion from that reference plane. Figure 4.14(c) and Figure 4.14(d) present the ratio using total and fluctuation fields considering the wall-parallel plane at different wall positions. These plots show the similar behaviour like 4.14(a) and Figure 4.14(b) with more significantly. Thus, the out of plane motions are much smaller scale than in plane motions.

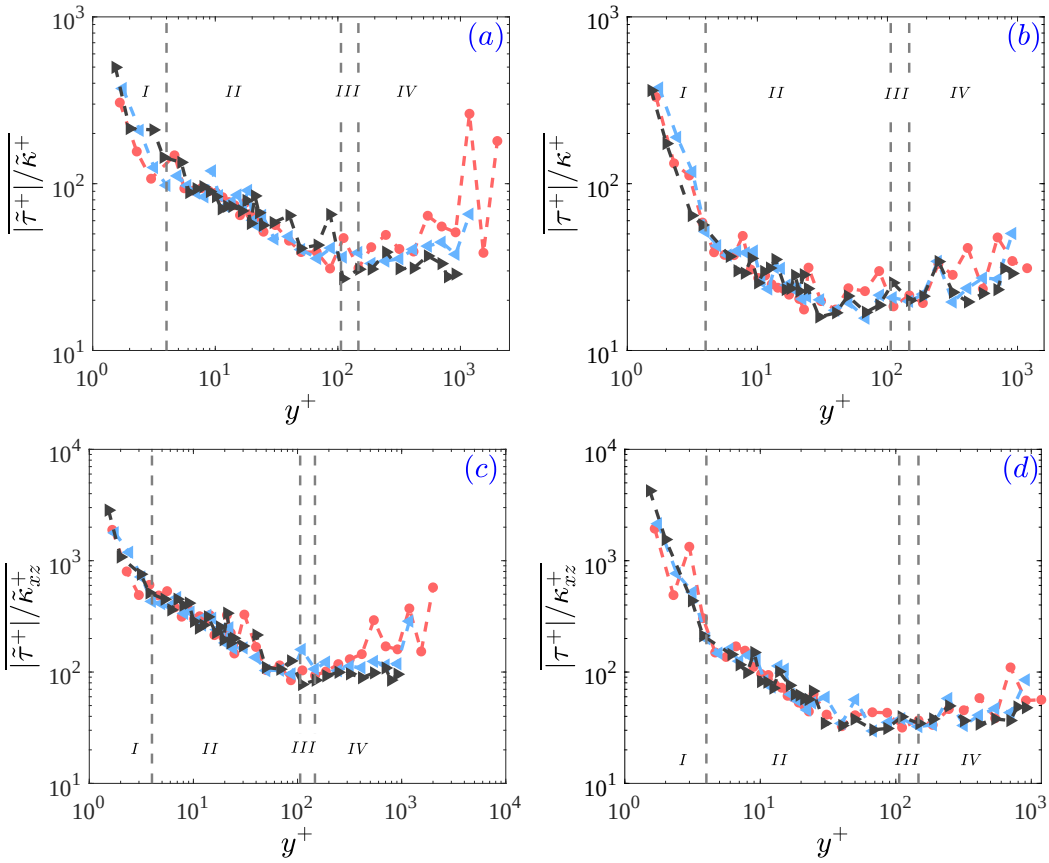

FIGURE 4.14: Ratio of τ and κ in case of the boundary layer (circle symbols are used for $\delta^+ \approx 2530$ and arrow symbols are for $\delta^+ \approx 1660$) and the channel flow (diamond symbols are used for $\delta^+ \approx 934$). The dashed lines represent the layer boundaries associated with the mean momentum equation (Table 1) corresponding to $\delta^+ = 1660$ for **(a)** for total velocity field, **(b)** for fluctuating velocity field

To analyse this potential intense twisting structure of the streamline and the curvature values around stagnation points, we now observe the joint statistics of curvature and torsion using fluctuation velocity field in the following section.

4.4 Joint probability density function

This section represents the joint statistics of the streamline geometries related to curvature and torsion. Here, we consider the fluctuating streamline pattern, with special attention on the streamline curvature and torsion behaviour near stagnation points $(u, v, w) \cong 0$. Figure 4.15 presents the joint probability density function of the fluctuating velocity magnitude $|\mathbf{V}| = \sqrt{u^2 + v^2 + w^2}$, and the inverse of fluctuating curvature magnitude, i.e. the radius of curvature, at four wall-positions in the four layers noted in table 1. Figure 4.15(a) shows the joint probability contour of $|\mathbf{V}^+|$ and $1/\kappa^+$ in near-wall region. Here, the peak of the radius of curvature $(1/\kappa^+)$ is weighted towards the minimum value of the velocity magnitude $(|\mathbf{V}^+|) \approx 0)$. This supports the notion that curvature values are maximal around stagnation points $(|\mathbf{V}^+|) \approx 0)$. This becomes more prevalent with distance from the wall as shown in figures 4.15(b)- (d) in layers II- IV respectively. This result physically agrees with the conclusion of Schaefer [2012] that extreme curvature values occur owing to sharply deflected streamlines in the vicinity of stagnation points.

Figure 4.16 shows the joint statistics of curvature and torsion for fluctuating streamlines pattern in four layers. This joint pdf is important to simplify the visualization of the vortical structure of turbulent flow. In the near-wall region, figure 4.16(a) shows the cone type contour that is weighted towards the negative torsion values jointly with the mean of the fluctuating curvature magnitude. Thus, near the wall, the mean bending region of the streamline corresponds the negative torsion values. Figures 4.16 (b) and (c) in layer II and III show that the joint pdfs are more likely circular type contours weighted towards the negative torsion values. Here, the twisting of the streamlines is grater around the mean bending region. Close to the channel centerline, figure 4.16(d) presents again a cone type contour as similar to figure 4.16(a). Here, the weighted torsion values in all layers are greater than the mean of the fluctuating curvature. Thus, the joint statistics of curvature and torsion again indicates the intense twisting pattern than bending for the vortical structures in the flow field.

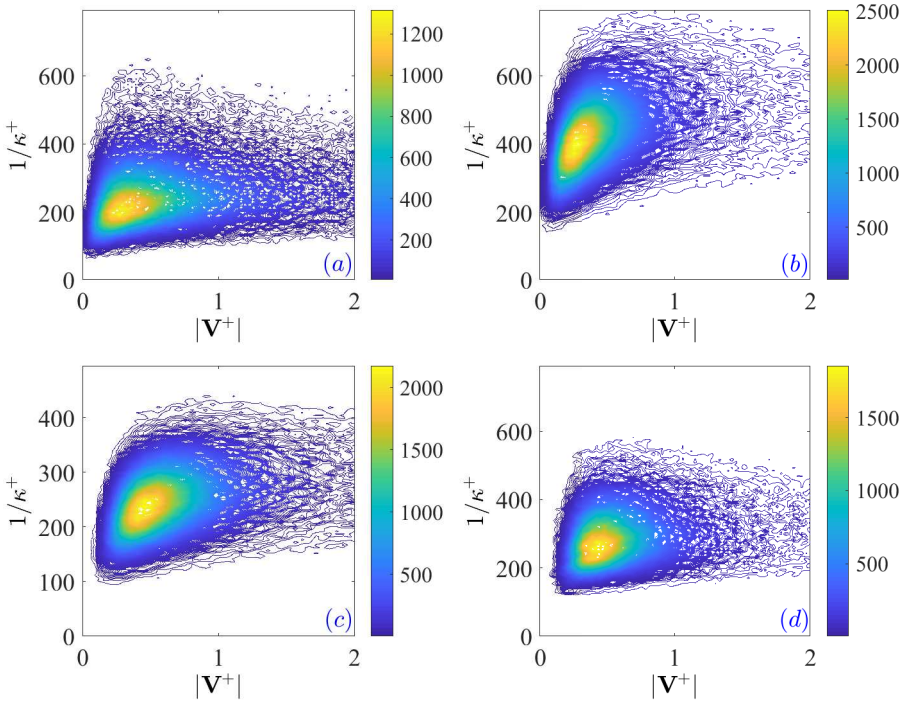

FIGURE 4.15: Joint pdf of the fluctuating velocity magnitude with the inverse of curvature magnitude for fluctuating streamlines pattern in case of the Channel flow at **(a)** $y^+ = 3$, **(b)** $y^+ = 30$, **(c)** $y^+ = 63$ and **(d)** $y^+ = 911$

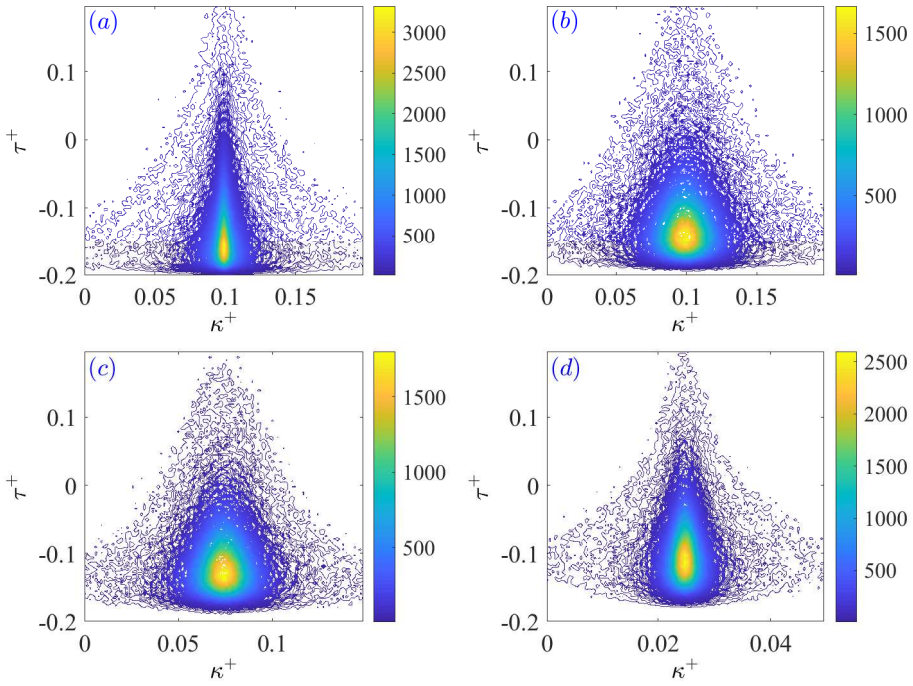

FIGURE 4.16: Joint pdf of fluctuating curvature and fluctuating torsion in case of the Channel flow at **(a)** $y^+ = 3$, **(b)** $y^+ = 30$, **(c)** $y^+ = 63$ and **(d)** $y^+ = 911$

4.4.1 Joint PDF of the curvature components

The orientation of the streamlines determines the curvature components. To understand the geometric characteristics of the streamlines in each layer of Table 1, joint pdfs of all three combinations for fluctuating κ_x, κ_y and κ_z were examined. In all cases, the pdfs show distortion due to the presence of the wall within $y^+ = 30$. This is reflected by non-circular contours. With increasing distance, however, the joint pdfs of κ_x^+, κ_z^+ and κ_y^+, κ_z^+ exhibit essentially circular pdfs centred about zero, yielding the correlation coefficient of about 0.01 or less (not shown here).

On the other hand, the joint distribution of κ_x^+, κ_y^+ in figure 4.17(a) shows the distorted pdfs concentrating in the second quadrant in layer I. This distortion most likely arises due to a combination of the viscous shear effect on κ_x^+ and wall-blocking effect on κ_y^+ as discussed earlier. Figure 4.17(b) in layer II also shows the distorted pdf that is weighted in the first and second quadrant. In layer III, figure 4.17(c) presents that the pdf is weighted in the first and second quadrant with the correlation coefficient, $R_{\kappa_x^+,\kappa_y^+} \cong -0.1$. Beyond this position and up to the centreline of the channel flow e.g. figure 4.17(d), the pdfs exhibit essentially circular contours centred about zero with $R_{\kappa_x^+,\kappa_y^+} \cong 0$. Here, κ_x^+ is more distorted than κ_y^+ before layer III. From layer III, the distortion owing to the shear along with the transfer of the mean shear into fluctuating vorticity diminishes. This dropping off the mean shear ends up the situation after $y^+ = 50$, where the enstrophy become turbulence as like isotropic flow. Thus, the considered wall-bounded flow cases innovate these results before the inertial layer due to the presence of the wall.

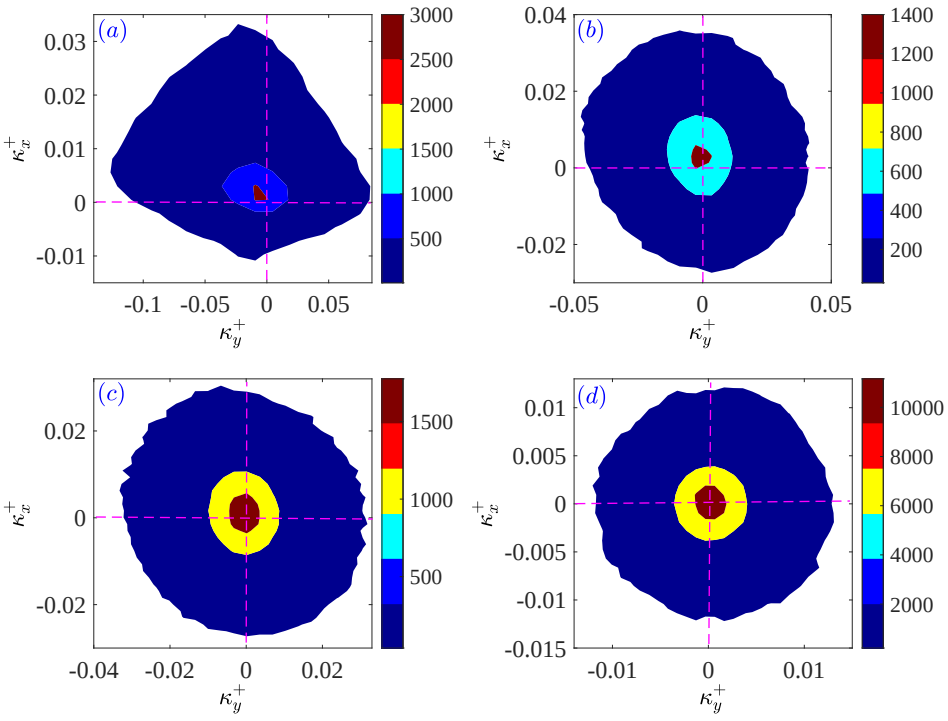

FIGURE 4.17: **(a)** Joint pdf of the streamwise curvature component with wall-normal curvature component for fluctuating streamlines pattern in case of the Channel flow at **(a)** $y^+ = 3$, **(b)** $y^+ = 30$, **(c)** $y^+ = 63$ and **(d)** $y^+ = 911$

4.5 Chapter summary

The present chapter described the statistical properties of the streamline geometries in turbulent flows. These streamline geometries relate to the local curvature (κ) and torsion (τ) and have been analysed using the DNS of channel and boundary layer flows. The streamlines of the flows were calculated using the 4th order Runge-Kutta method. The Frenet-Serret formulas from differential geometry were used to establish the equations for κ and τ. Curvature is calculated using the tangent vectors and the arc length of the corresponding streamline curve. Torsion is calculated using central difference formulas for the derivative terms in the definitional equation of τ. The variation of the mean statistics of curvature magnitude ($\overline{\kappa}$) and curvature components ($\overline{\kappa_x}, \overline{\kappa_y}, \overline{\kappa_z}$) with wall-normal locations have been explained previously and are not repeated in detail here. Curvature statistics show some interesting behaviour close to the wall, and between $y^+ \simeq 17$ (the peak location of the turbulent kinetic energy) and $y^+ \simeq 50$. Here, at $y^+ \simeq 50$, vorticity advection leads to the spatial dispersion of vorticity that increasingly dominates with increasing y^+ [Klewicki, 2013*a*]. In the classical log layer, the radius of curvature exhibits a power law variation that varies similarly to the Taylor microscale. An interesting result from the mean statistics is the positive peak of $\overline{\kappa_y}$ that appears close to the wall. To understand this peak result of $\overline{\kappa_y}$ physically, the correlation coefficient of v and κ_y and the conditional average of v field corresponding to positive κ_y were computed. The results show an anti-correlation between v and κ_y except close to the wall. All these results support that the positive $\overline{\kappa_y}$ peak is associated with a strong negative v followed by a weaker positive v. In other words, the positive peak near the wall is related to the strong wallward streamline. The maximum variance of curvature corresponding to the mean occurs close to the wall and close to the channel centreline. This is revealed using the ratio of mean curvature to its standard deviation.

The pdfs of the curvature magnitude and the curvature components with an exponent of -4 scaling have been shown for both total and fluctuating velocity fields. From the pdf plot for the fluctuating curvature magnitude, it is apparent that -4 scaling is predominant at increasing distances from the wall. The -4 scaling is relevant to describe the extreme curvature values near stagnation points [Schaefer, 2012] (see figure 4.18). The onset of this scaling has been compared with the inverse of the Kolmogorov length scale at different wall positions which varies as $1/y^+$ in the inertial domain (logarithmic layer). This is consistent with the linearly decreasing number density of stagnation points with y^+ in the inertial layer [Dallas *et al.*, 2009]. The interesting results we observe include, the onset of -4 scaling varies inversely with the Kolmogorov scale and the radius of curvature varies proportionally with the Taylor microscale in the inertial layer, where these results follow $1/y^+$ in the same domain. The non-proportional results before $y^+ \lesssim 50$ arise from the wall-blocking effect within $y^+ \approx 30$, and from the viscous effect within $30 \leqslant y^+ \leqslant 50$. This assertion is reinforced by analysing the positive and negative pdf profiles of the wall-normal curvature, and the joint pdfs of curvature components. In addition, the contours of the total and fluctuating velocity fields

with corresponding streamlines show the mean subtraction effect on the streamline pattern physically.

The properties of the out of plane motion of the streamlines have been shown by the mean and the standard deviation statistics of torsion. The ratio of torsion to the curvature reveals that the out of plane pattern is smaller scale than the in-plane pattern for both total and fluctuating streamline patterns. The joint pdf results describe the streamline pattern and behaviour close to the stagnation points as shown in figure 4.18.

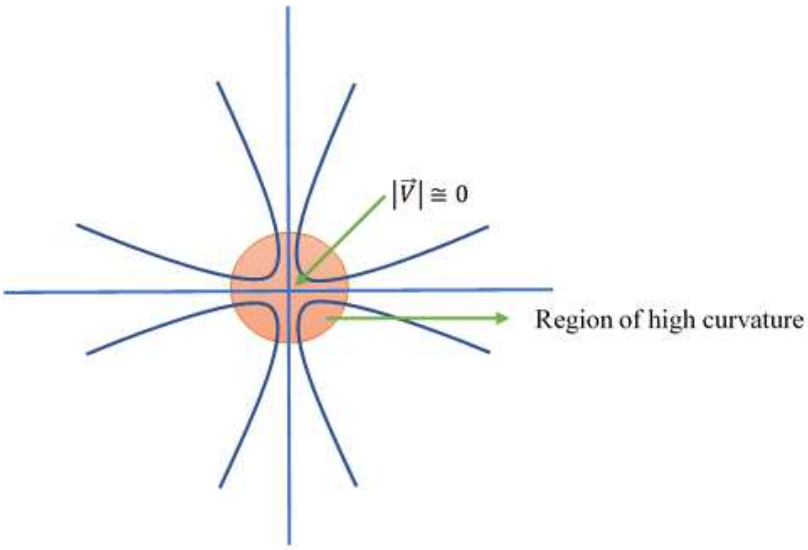

FIGURE 4.18: Sketch of streamlines near a stagnation point

To summarize, the high curvature values are associated with the stagnation points, where streamlines are sharply deflected as displayed in figure 4.18. In the inertial domain, the density of the stagnation point decays linearly with y^+ with the strength decay of the vortical motion Klewicki [2013*a*]. In this domain, the dominating mechanism of the vorticity intensity underlying the spatial dispersion of the vorticity, increases with developing y^+. The onset of -4 scaling of curvature is proportional to the inverse Kolmogorov scale in the same domain, where the radius of curvature scales similar to Taylor microscale, whereas all these follow $1/y^+$. These results are likely to have connection to the evolution of the vortical motions and their spatial structure with distance from the wall.

Chapter 5

Conclusions

5.1 Summary of the main findings

In a broad sense, while the present research aims to find the potential relationship between the geometrical and dynamical properties of the wall-bounded turbulence, this thesis is mostly related to the statistics for the geometrical properties of wall-bounded turbulence. The principal findings of this research can be described by two main sections; (*i*) The statistical properties of the streamline geometry related to curvature and torsion, and (*ii*) The connection of these statistical properties to the previous literature. Although streamline geometry related to curvature and torsion has been studied prior to this research, none of those studies have focused on wall-bounded turbulent flows. Furthermore, the Reynolds number range (≈ 934 to ≈ 2000) and data density (35 wall-normal locations per profile) are unique to the present research. The relevant literature has been discussed in chapter 2 and the rest of the chapters are based on the aims stated in chapter 1. The key findings are summarized here.

5.1.1 Calculation technique

The present study employs DNS data sets for boundary layers (Reynolds numbers $\approx 1310, 2000$) and channel flow (Reynolds number ≈ 934) cases. Streamlines are calculated using a 4th order Runge-Kutta method starting from each grid point. The step size between two points on the streamline is 0.14 viscous unit according to the present consideration. Curvature and torsion of a streamline are defined by using the Frenet-Serret formulas from differential geometry in terms of tangent, normal and binormal vectors. Curvature and torsion are calculated locally i.e., at the starting point for each streamline. The Matlab codes for the present curvature and torsion calculation have been verified by the known results in case of straight line, circle and helix curve.

5.1.2 Statistics of streamline geometry

The statistics of streamline geometry related to curvature and torsion exhibits both decreasing and increasing trends with wall-normal positions. Curvature statistics shows some interesting behaviour close to the wall, and in the region between $17 \lesssim y^+ \lesssim 50$. In the classical log layer, the radius of curvature exhibits a power-law variation that varies similarly to the Taylor microscale. An interesting result from the mean statistics is the positive peak of wall-normal curvature that appears close to the wall. To understand this result physically, the conditional average of wall-normal velocity field corresponding to positive wall-normal curvature and the correlation coefficient between these quantities were computed. All these results support that the near-wall positive wall-normal curvature peak is associated with the strong wall-ward flow followed by the weak away from the wall streamline pattern. Moreover, the maximum variance of curvature corresponding to the mean occurs close to the wall and close to the channel centreline.

The probability density functions (pdfs) of the curvature magnitude and the curvature components show a power-law behaviour of $P(\kappa) \sim \kappa^{-4}$ for both total and fluctuating velocity fields for large curvature magnitudes. This scaling for fluctuating curvature is predominant with increasing distances from the wall. The -4 scaling is relevant to describing the extreme curvature values near stagnation points [Schaefer, 2012] (see figure 4.18). The curvature value at the onset of this scaling compares well with the inverse of the Kolmogorov length scale at different wall positions which in turn varies inversely with y^+ in the inertial domain (logarithmic layer). This is also consistent with the linearly decreasing number density of stagnation points with y^+ in the inertial layer [Dallas *et al.*, 2009]. Here, the interesting results we observe thus include, the onset of -4 scaling varies inversely with the Kolmogorov scale and the radius of curvature varies proportionally with the Taylor microscale in the inertial layer. The non-proportional results before the inertial layer arise partially due to the wall-blocking and the viscous effect, and then outside the viscous wall layer the results begin to appear similar to those in isotropic flow. This results are verified by the positive and negative wall-normal curvature pdf profiles and the joint pdfs of curvature components.

The properties of the out of plane motion of the streamlines have been shown by the mean and the standard deviation statistics of torsion. The ratio of torsion to curvature suggest a strong relative tendency for streamline to move out of wall-parallel planes.

5.1.3 Connections to the prior literature

All the background literature draws a significant connection to the present study. The reorientation mechanism for vorticity stretching and advection studied by Klewicki [2013*a*], is reflected by the present mean curvature statistics. As analysed by Schaefer [2012], the curvature values are extreme around stagnation points and follow an exponent of -4 scaling. According to the studies by Vassilicos and

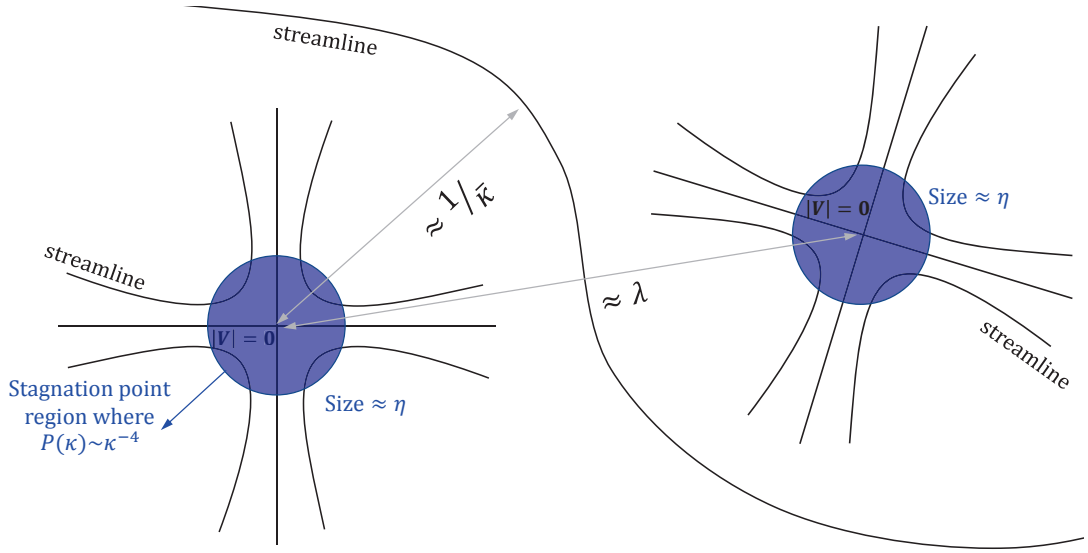

FIGURE 5.1: Sketch of streamlines around a pair of stagnation points. The spacing between these points are $\approx \lambda$, whereas the bounding turbulent motion has a size of $1/\overline{\kappa}$. The region close to the stagnation points of size η is where we expect the curvature pdf $P(\kappa) \sim \kappa^{-4}$ scaling.

co-workers [Dallas *et al.*, 2009, Goto & Vassilicos, 2009], the number density of the stagnation points decrease with y^+ in the inertial domain where the distance between stagnation points is proportional to the Taylor microscale. The present study shows that the onset of -4 scaling varies proportionally with the inverse of Kolmogorov scale following $1/y^+$ in the inertial domain. Whereas in the same domain, the radius of curvature follows the Taylor microscale. These results are likely to have a connection to the evolution of the vortical motions and their spatial structure with distance from the wall.

5.2 Suggestions for future works

As discussed earlier, the broad aim of the research is to clarify mechanisms underlying the apparent connections between geometry and dynamics in case of wall-bounded flow, and the degree to which they are reflected in the instantaneous motions. This thesis discusses the statistical properties of streamline geometry related to curvature and torsion while the dynamics of the wall-flow have been analysed in the previous literature. Thus a few suggestions for possible extensions to the current work include the following.

The advective term of the Navior-Stockes equation has a mathematically well-defined relationship with the streamline curvatures (Schaefer [2012]). From this relationship, the author has observed that the Reynolds stress term of the mean momentum equation (Wei *et al.* [2005]) can be presented by the curvature components along with velocity and tangent vectors. Therefore, the dynamics in the inertial region can be mathematically connected to the properties of the curvature

and thus related to the momentum transporting motion. Further study of these connection would seem worthwhile.

Appendix A

Streamline calculation technique

A.1 Runge-Kutta Method for calculating streamline

We use a 4th order Runge-Kutta method to compute the streamline starting at each grid point of a DNS flow volume. Here, the 3rd derivative is the highest derivative in the curvature and torsion definitions (equation 3.8 and 3.12), which requires the maximum seven point to use the central difference formula in equation 3.15. Therefore, we use the Runge-Kutta method to calculate a portion of the streamline. If a streamline starts at the grid point (x_0, y_0, z_0), then the first point on the streamline (x_1, y_1, z_1) is the grid point itself i.e.,

$$x_1 = x_0, y_1 = y_0, z_1 = z_0. \tag{A.1}$$

Using the streamwise u, wall-normal v and spanwise w velocities, the increments $k1_x$, $k1_y$, and $k1_z$, based on the slopes at the initial point at the beginning of the time step h (discussed in the next section) are calculated. If we use the increments $k1_x$, $k1_y$, and $k1_z$ to the halfway through the time step, then $k2_x$, $k2_y$, and $k2_z$ are the estimations of the slopes at the midpoint. These slopes are more accurate than $k1_x$, $k1_y$, and $k1_z$ for making new approximations of the point (x_1, y_1, z_1). Thus the new approximation of the point (x_1, y_1, z_1) is:

$$\begin{aligned} x1_a &= x_1 + k1_x.(h/2), \\ y1_a &= y_1 + k1_y.(h/2), \\ z1_a &= z_1 + k1_z.(h/2), \end{aligned} \tag{A.2}$$

and $k2_x$, $k2_y$, and $k2_z$ are calculated using the point $(x1_a, y1_a, z1_a)$. If we use the increment $k2_x$, $k2_y$, and $k2_z$ to the halfway through the time step, then $k3_x$, $k2_y$, and $k3_z$ are the estimations of the slopes at the midpoint. Thus, the new

approximation of the point (x_1, y_1, z_1) is:

$$\begin{aligned} x1_b &= x_1 + k2_x.(h/2), \\ y1_b &= y_1 + k2_y.(h/2), \\ z1_b &= z_1 + k2_z.(h/2), \end{aligned} \tag{A.3}$$

and $k3_x$, $k3_y$, and $k3_z$ are calculated using the point $(x1_b, y1_b, z1_b)$. Finally, we use the increment, $k3_x$, $k3_y$, and $k3_z$ to all the way across the time step, and then $k4_x$, $k4_y$, and $k4_z$ are the estimations of the slopes at the endpoint. Thus, the approximation of the point (x_1, y_1, z_1) is:

$$\begin{aligned} x1_c &= x_1 + k3_x.(h), \\ y1_c &= y_1 + k3_y.(h), \\ z1_c &= z_1 + k3_z.(h), \end{aligned} \tag{A.4}$$

and $k4_x$, $k4_y$, and $k4_z$ are calculated using the point $(x1_c, y1_c, z1_c)$. Now, using the 4th order Runge-Kutta method, the sum of these slopes gives the next point on the streamline

$$\begin{aligned} x_2 &= x_1 + (h/6).(k1_x + 2.k2_x + 2.k3_x + k4_x), \\ y_2 &= y_1 + (h/6).(k1_y + 2.k2_y + 2.k3_y + k4_y), \end{aligned}$$

and

$$z_2 = z_1 + (h/6).(k1_z + 2.k2_z + 2.k3_z + k4_z). \tag{A.5}$$

Similarly, for calculating next point (x_3, y_3, z_3) on the streamline, we take (x_2, y_2, z_2) as the initial point and follow the above procedure from equation A.1-A.5. Thus we can calculate as many points on the streamline as required. In this case, we compute the first seven points on the streamline as it is sufficient for the curvature and torsion calculation. A schematic diagram for calculating streamline is presented in figure A.1. In reality, the red grid points, and the blue points on the streamline are very close to each other. The distance between two points on the streamline i.e. the step size $h = 0.001$ (discussed in the next section). For this very small distance, the central difference formula could be applied at the 4th point on the streamline to calculate local curvature and torsion at the first point on the streamline.

A.1.1 Preliminary results for comparison

In this section, we compare the curvature statistics computed using the calculation method for equations 3.8 and 3.21. Figure A.2 shows the mean and standard deviation curvature at different wall positions. The profiles show exactly the same

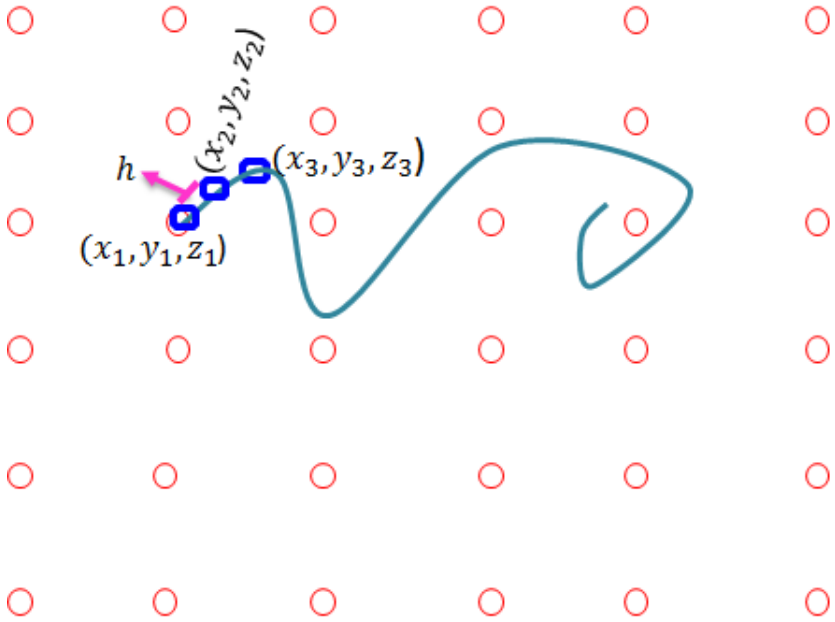

FIGURE A.1: Schematic diagram of a streamline calculation using the 4th order Runge-Kutta method. Red circles present the grid points of a flow field, small blue rectangles show the points on the streamline (solid blue line), and h is the step size between two pints on the streamline.

results for these two curvature definitions. We choose the vector method (equation 3.21) for curvature calculation as it also includes the curvature components definitions.

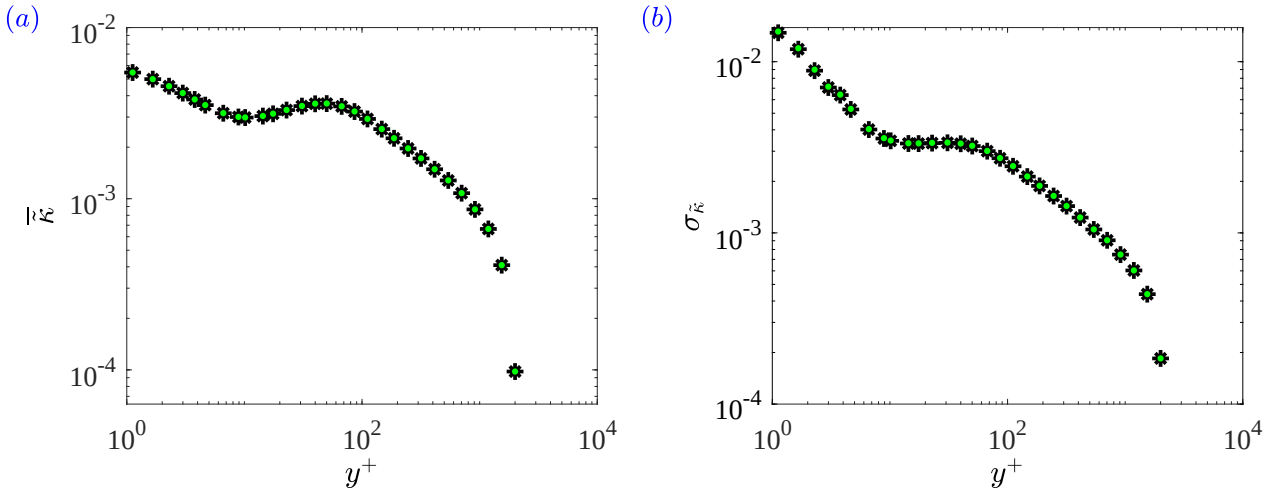

FIGURE A.2: Comparison of two methods for curvature calculation. Black cross symbols denote the data using equation 3.8 and that's of green dots using equation 3.21. **(a)** mean and **(b)** standard deviation at different wall positions

Bibliography

Braun, W., De Lillo, F. & Eckhardt, B. 2006 Geometry of particle paths in turbulent flows. *J. Turbulence* (7), N62.

Chauhan, K. A., Monkewitz, P. A. & Nagib, H. M. 2009 Criteria for assessing experiments in zero pressure gradient boundary layers. *Fluid Dynamics Research* **41** (2), 021404.

Dallas, V., Vassilicos, J. C. & Hewitt, G. F. 2009 Stagnation point von Kármán coefficient. *Phys. Review E* **80** (4), 046306.

Del Alamo, J. C., Jiménez, J., Zandonade, P. & Moser, R. D. 2004 Scaling of the energy spectra of turbulent channels. *J. Fluid Mech.* **500**, 135–144.

Eyink, G. L. 2008 Turbulent flow in pipes and channels as cross-stream "inverse cascades" of vorticity. *Phys. Fluids* **20** (12), 125101.

Fife, P., Wei, T., Klewicki, J. & McMurtry, P. 2005 Stress gradient balance layers and scale hierarchies in wall-bounded turbulent flows. *J. Fluid Mech.* **532**, 165–189.

Goto, S. & Vassilicos, J. C. 2009 The dissipation rate coefficient of turbulence is not universal and depends on the internal stagnation point structure. *Phys. Fluids* **21** (3), 035104.

Huerre, P. & Monkewitz, P. A. 1990 Local and global instabilities in spatially developing flows. *Ann. Rev. Fluid Mech.* **22** (1), 473–537.

Jeong, J., Hussain, F., Schoppa, W. & Kim, J. 1997 Coherent structures near the wall in a turbulent channel flow. *J. Fluid Mech.* **332**, 185–214.

Johansson, A. V, Alfredsson, P H. & Kim, J. 1991 Evolution and dynamics of shear-layer structures in near-wall turbulence. *J. Fluid Mech* **224**, 579–599.

Klewicki, J. 2010 Reynolds number dependence, scaling, and dynamics of turbulent boundary layers. *J. Fluids Eng.* **132** (9), 094001.

Klewicki, J. 2013*a* A description of turbulent wall-flow vorticity consistent with mean dynamics. *J. Fluid Mech.* **737**, 176–204.

Klewicki, J. 2013*b* Self-similar mean dynamics in turbulent wall flows. *J. Fluid Mech.* **718**, 596–621.

Klewicki, J. & Falco, R. 1990 On accurately measuring statistics associated with small-scale structure in turbulent boundary layers using hot-wire probes. *J. Fluid Mech.* **219**, 119–142.

Klewicki, J., Fife, P. & Wei, T. 2009 On the logarithmic mean profile. *J. Fluid Mech.* **638**, 73–93.

Klewicki, J., Fife, P., Wei, T. & McMurtry, P. 2007 A physical model of the turbulent boundary layer consonant with mean momentum balance structure. *Philosophical Transactions of the Royal Society of London A: Mathematical, Physical and Engineering Sciences* **365** (1852), 823–840.

Klewicki, J. & Hirschi, C. 2004 Flow field properties local to near-wall shear layers in a low Reynolds number turbulent boundary layer. *Phys. Fluids* **16** (11), 4163–4176.

Klewicki, J. & Oberlack, M. 2015 Finite Reynolds number properties of a turbulent channel flow similarity solution. *Phys. Fluids* **27** (9), 095110.

Klewicki, J., Philip, J., Marusic, I., Chauhan, K. & Morrill-Winter, C. 2014 Self-similarity in the inertial region of wall turbulence. *Phys. Review E* **90** (6), 063015.

Marusic, I., McKeon, B. J., Monkewitz, P. A., Nagib, H., Smits, A. & Sreenivasan, K. 2010 Wall-bounded turbulent flows at high Reynolds numbers: recent advances and key issues. *Phys. Fluids* **22** (6), 065103.

Marusic, I., Monty, J. P., Hultmark, M. & Smits, A. J. 2013 On the logarithmic region in wall turbulence. *J. Fluid Mech.* **716**.

Mazellier, N. & Vassilicos, J. C. 2008 The turbulence dissipation constant is not universal because of its universal dependence on large-scale flow topology. *Phys. Fluids* **20** (1), 015101.

Meneveau, C. & Marusic, I. 2013 Generalized logarithmic law for high-order moments in turbulent boundary layers. *J. Fluid Mech.* **719**.

Millman, R. S. & Parker, G. D. 1977 *Elements of differential geometry*.

Morrill-Winter, C & Klewicki, J 2013 Influences of boundary layer scale separation on the vorticity transport contribution to turbulent inertia. *Phys. Fluids* **25** (1), 015108.

Morrill-Winter, C., Philip, J. & Klewicki, J. 2017*a* An invariant representation of mean inertia: theoretical basis for a log law in turbulent boundary layers. *J. Fluid Mech.* **813**, 594–617.

Morrill-Winter, C., Philip, J. & Klewicki, J. 2017*b* Statistical evidence of anasymptotic geometric structure to the momentum transporting motions in turbulent boundary layers. *Phil. Trans. R. Soc. A* **375** (2089), 20160084.

Perry, A. E. & Chong, M. S. 1982 On the mechanism of wall turbulence. *J. Fluid Mech.* **119**, 173–217.

Peters, N., Wang, L., Mellado, J.-P., Gobbert, J. H., Gauding, M., Schafer, P. & Gampert, M. 2010 Geometrical properties of small scale turbulence. In *John von Neumann Inst. for Computing NIC Symposium*, pp. 365–371.

Priyadarshana, P., Klewicki, J., Treat, S. & Foss, J. 2007 Statistical structure of turbulent-boundary-layer velocity–vorticity products at high and low Reynolds numbers. *J. Fluid Mech.* **570**, 307–346.

Robinson, S. K. 1991 Coherent motions in the turbulent boundary layer. *Ann. Rev. Fluid Mech.* **23** (1), 601–639.

Scagliarini, A. 2011 Geometric properties of particle trajectories in turbulent flows. *J. Turbulence* (12).

Schaefer, P. 2012 Curvature statistics of streamlines in various turbulent flows. *J.Turbulence* (13), N28.

Schaefer, P., Gampert, M. & Peters, N. 2012 The length distribution of streamline segments in homogeneous isotropic decaying turbulence. *Phys. Fluids* **24** (4), 045104.

Sharma, A. & McKeon, B. 2013 On coherent structure in wall turbulence. *J. Fluid Mech.* **728**, 196–238.

Sillero, J. A., Jiménez, J. & Moser, R. D. 2013 One-point statistics for turbulent wall-bounded flows at reynolds numbers up to $\delta^+ \approx 2000$. *Phys. Fluids* **25** (10), 105102.

Smits, A. J, McKeon, B. J & Marusic, I. 2011 High–Reynolds number wall turbulence. *Ann. Rev. Fluid Mech.* **43**.

Sreenivasan, KR, Prabhu, A & Narasimha, R 1983 Zero-crossings in turbulent signals. *J. Fluid Mech.* **137**, 251–272.

Tennekes, H. & Lumley, J. L. 1972 *A first course in turbulence*. MIT press.

Townsend, A. A. 1976 *The structure of turbulent shear flow*. Cambridge university press.

Vincenti, P., Klewicki, J., Morrill-Winter, C., White, C. & Wosnik, M. 2013 Streamwise velocity statistics in turbulent boundary layers that spatially develop to high Reynolds number. *Exp. fluids* **54** (12), 1629.

Wang, L. 2010 On properties of fluid turbulence along streamlines. *J. Fluid Mech.* **648**, 183–203.

Wei, T., Fife, P., Klewicki, J. & McMurtry, P. 2005 Properties of the mean momentum balance in turbulent boundary layer, pipe and channel flows. *J. Fluid Mech.* **522**, 303–327.

Wu, J-Z, Ma, H-Y & Zhou, M-D 2007 *Vorticity and vortex dynamics*. Springer Science & Business Media.

Zhou, A. & Klewicki, J. 2015 Properties of the streamwise velocity fluctuations in the inertial layer of turbulent boundary layers and their connection to self-similar mean dynamics. *Int. J. Heat and Fluid Flow* **51**, 372–382.